

## Existence and stability of marginally trapped surfaces in black-hole spacetimes

Daniel Pook-Kolb,<sup>1,2</sup> Ofek Birnholtz,<sup>3</sup> Badri Krishnan,<sup>1,2</sup> and Erik Schnetter<sup>4,5,6</sup>

<sup>1</sup>*Max-Planck-Institut für Gravitationsphysik (Albert Einstein Institute),  
Callinstrasse 38, 30167 Hannover, Germany*

<sup>2</sup>*Leibniz Universität Hannover, 30167 Hannover, Germany*

<sup>3</sup>*Center for Computational Relativity and Gravitation, Rochester Institute of Technology,  
170 Lomb Memorial Drive, Rochester, New York 14623, USA*

<sup>4</sup>*Perimeter Institute for Theoretical Physics, Waterloo, Ontario N2L 2Y5, Canada*

<sup>5</sup>*Physics and Astronomy Department, University of Waterloo, Waterloo, Ontario N2L 3G1, Canada*

<sup>6</sup>*Center for Computation and Technology, Louisiana State University,  
Baton Rouge, Louisiana 70803, USA*



(Received 3 December 2018; published 6 March 2019)

Marginally outer trapped surfaces (MOTSs, or marginal surfaces in short) are routinely used in numerical simulations of black-hole spacetimes. They are an invaluable tool for locating and characterizing black holes quasilocally in real time while the simulation is ongoing. It is often believed that a MOTS can behave unpredictably under time evolution; an existing MOTS can disappear, and a new one can appear without any apparent reason. In this paper we show that in fact the behavior of a MOTS is perfectly predictable and its behavior is dictated by a single real parameter, the *stability parameter*, which can be monitored during the course of a numerical simulation. We demonstrate the utility of the stability parameter to fully understand the variety of marginal surfaces that can be present in binary black-hole initial data. We also develop a new horizon finder capable of locating very highly distorted marginal surfaces and we show that even in these cases, the stability parameter perfectly predicts the existence and stability of marginal surfaces.

DOI: [10.1103/PhysRevD.99.064005](https://doi.org/10.1103/PhysRevD.99.064005)

### I. INTRODUCTION

Numerical solutions of Einstein's equations (with and without matter) are an important tool in gravitational wave astronomy (see e.g., [1–9]). In situations without any symmetries or without any preferred background solution, these numerical solutions are typically the most accurate and are frequently used as benchmarks against which various approximation methods can be tested. In simulations of black-hole spacetimes, computing the gravitational wave signal is only one part of the solution. It is important to characterize the black holes as well. For example, in a binary black-hole merger, one would like to track the location and velocity of the black holes, and their physical properties such as mass, angular momentum and higher multipole moments. Similarly, when the black holes merge and the final black hole is formed, one would like to know when a common horizon forms and what the properties of the final black hole are.

In numerical simulations, one typically uses marginally trapped surfaces to answer these questions. Previous numerical methods for locating marginal surfaces are described in [10–16]. As we shall define in more detail later, these are closed two-dimensional surfaces with the topology of a sphere, in a time slice. They have the property

that the outgoing light rays emanating from them in the normal outward direction have vanishing expansion. The outermost such surface at a given time is called the apparent horizon. Through the Penrose-Hawking singularity theorems, the presence of such surfaces, together with various energy conditions, indicates the presence of a singularity in the future [17,18]. While not the main focus of this paper, the notion of a marginally outer trapped surface (MOTS) also forms the starting point for the study of quasilocal black-hole horizons. If a MOTS evolves smoothly in time, we can consider the smooth 3-manifold  $\mathcal{H}$  formed by stacking up the MOTSs at different times. Several important results hold for this world tube  $\mathcal{H}$  in different situations. For example, one can formulate the laws of black-hole mechanics, define multipole moments, obtain balance laws for the area and multipole moments, and calculate black-hole entropy in quantum gravity; see e.g., [19–25]. The applications of most relevance for us are in numerical relativity where they are regularly used to assign mass, angular momentum and higher multipole moments to black holes (see e.g., [26–28]).

The alternative to MOTSs and quasilocal horizons are event horizons. Many of the classic results of black-hole physics, such as the area increase law, black-hole

thermodynamics, etc., were initially based on event horizons (see e.g., [29–33]). However, the global and teleological nature of event horizons are well known. For both practical and theoretical reasons, event horizons are not ideal for extracting the parameters of black holes. First, their teleological nature makes it impossible to locate them in real time in a numerical simulation (or an experiment); we need to know the entire spacetime. Furthermore, it is primarily in perturbative situations that event horizons are useful for defining and extracting parameters like black-hole mass, spin, etc. In more general situations far from stationarity, such as during a binary black-hole merger, event horizons are not suitable for this purpose. For example, it is easy to construct examples where event horizons form and grow in flat Minkowski space where there should be no flux of gravitational radiation. These issues are discussed in more detail elsewhere (see e.g., [19,20,34–37]).

Despite the utility of marginal surfaces, there still remain many doubts about their behavior under time evolution. It is observed that apparent horizons can jump discontinuously. This jump is now well understood to arise from the outermost condition for apparent horizons, and the underlying marginal surfaces are observed to evolve smoothly [23,27,38,39]. It is still not clear if this would also hold for highly distorted marginal surfaces. Do highly distorted marginal surfaces still continue smoothly? Is there a quantifiable way in which one can say that a more distorted MOTS is more unstable? There are cases when a marginal surface can no longer be found. Is this due to problems with the horizon finders or is it really that the marginal surface has ceased to exist? Apart from their intrinsic interest, answers to such questions are important to ensure the reliability of various physical quantities that are routinely calculated in numerical simulations.

At any given time, there can exist several marginally trapped surfaces in a binary black-hole spacetime. This may include the two related with the two individual black holes, and possibly two more, related to the common final black hole (if it has formed). The outermost of these is called the apparent horizon but the other marginally trapped surfaces are of interest as well [see e.g., Fig. 1(b) below for an example]. At late times, the apparent horizon will usually approach the event horizon (see however [40,41]) but the fate of the other marginal surfaces in the interior is not yet fully understood. This question is also of relevance for understanding the “issue of the final state.” Mathematically this refers to the question of nonlinear stability of Kerr black holes. Astrophysically, restricting ourselves to binary systems, it refers to the fact that at late times, irrespective of the initial configuration, the end state is a Kerr black hole in equilibrium. The exterior spacetime, and how the gravitational wave signal shows this approach to equilibrium, and also how the horizon approaches equilibrium have been previously studied. The structure

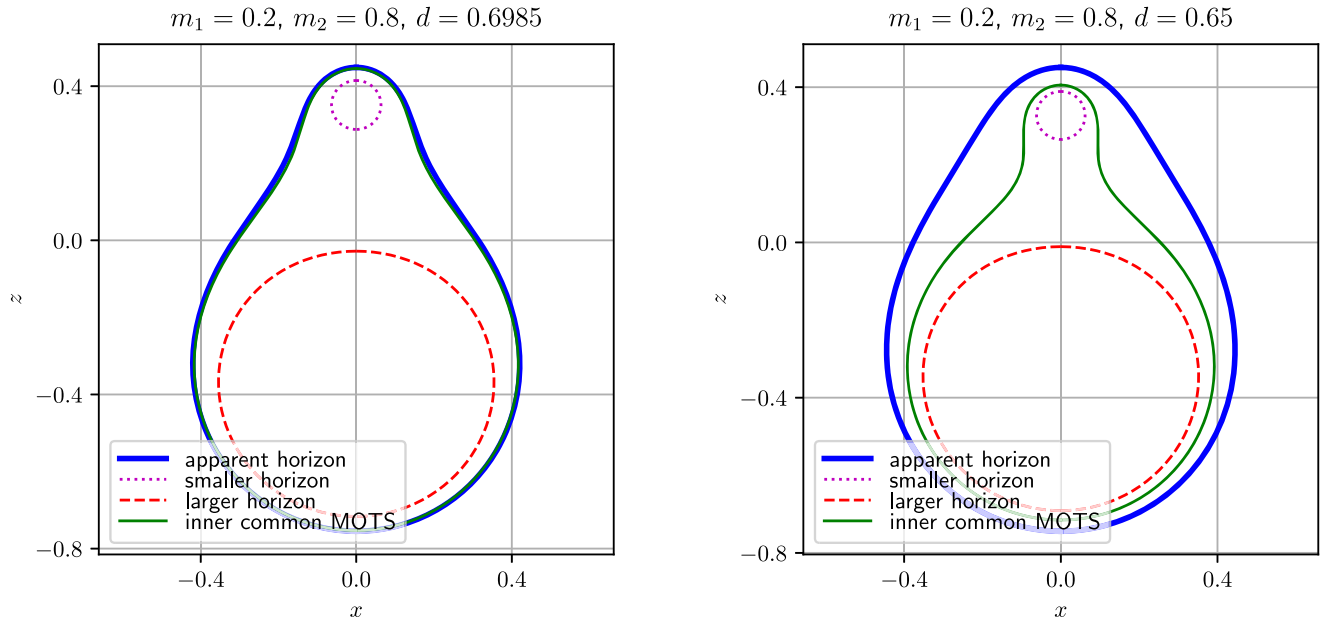
of the interior is unresolved and the behavior of the interior marginal surfaces is much less understood.

It might be argued that understanding the interior spacetime is of no physical interest since this region is causally disconnected from the external world where observations can be made—but this is incorrect. Physical phenomena in the interior and in the exterior regions are both a result of dynamics and nonlinearities occurring outside the event horizon. Thus, we expect the two regions to be correlated and, in fact, such correlations have been shown to exist [28,42–45]. The existence of these correlations leads to the interesting possibility of inferring properties of the interior spacetime from gravitational wave observations. Thus, even from an astrophysical perspective, it becomes important to understand the interior spacetime in detail.

Mathematically, the conditions under which a marginal surface evolves smoothly are known. Andersson *et al.* [46–49] have shown that the key object for understanding these issues is the *stability operator*. This is a second-order elliptic, possibly non-self-adjoint differential operator defined on every MOTS. If its smallest eigenvalue (which is guaranteed to be real) is positive, then the MOTS evolves smoothly in time. Much less is known rigorously for the cases when the principal eigenvalue is negative. In these cases, the world tube swept out by the MOTSs is not spacelike; this is studied in [50,51]. To our knowledge, this stability operator has never been used in a numerical calculation so far. In this paper we demonstrate the utility of the stability operator in numerical relativity, even for unstable and extremely distorted marginal surfaces.

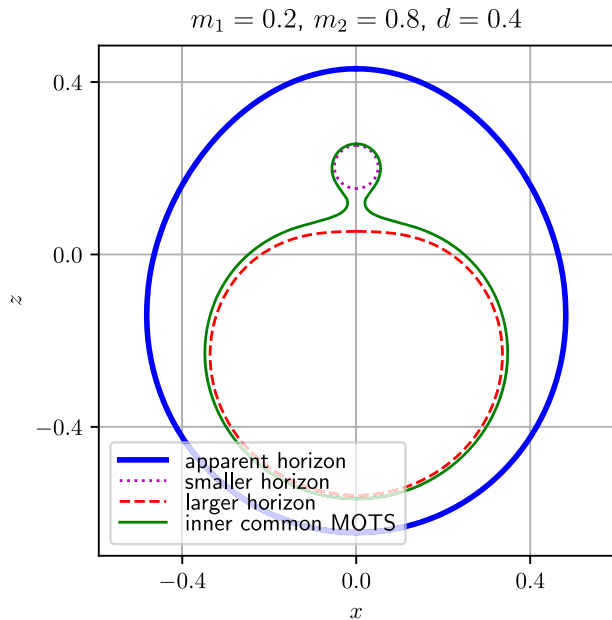
In order to really test the utility of the stability operator, we need to calculate it for marginal surfaces which are extremely distorted. The difficulty is that current horizon finders are generally not capable of locating highly distorted surfaces. The most commonly used numerical algorithms make certain assumptions on the marginal surfaces they are trying to locate [52]. For example, the AHFinderDirect method available in the Einstein Toolkit [15,53,54] assumes that the surface can be represented by a single-valued function  $h(\theta, \phi)$  of the usual angles  $(\theta, \phi)$  in some spherical coordinate system. When this condition is satisfied, then the marginal surface equation can be cast as an elliptic equation for  $h(\theta, \phi)$  which can be solved efficiently. This condition requires that any ray drawn from the origin of coordinates intersects the surface exactly once, and a surface satisfying this condition is said to be *star shaped*. It is not expected that marginal surfaces should always satisfy this condition, and we shall study explicit counterexamples below. The second goal of this paper is thus the development and implementation of a new numerical method for finding marginal surfaces which is computationally as fast as AHFinderDirect yet is capable of finding arbitrarily distorted surfaces.

Armed with our new horizon finder, we investigate with high numerical precision the various marginal surfaces

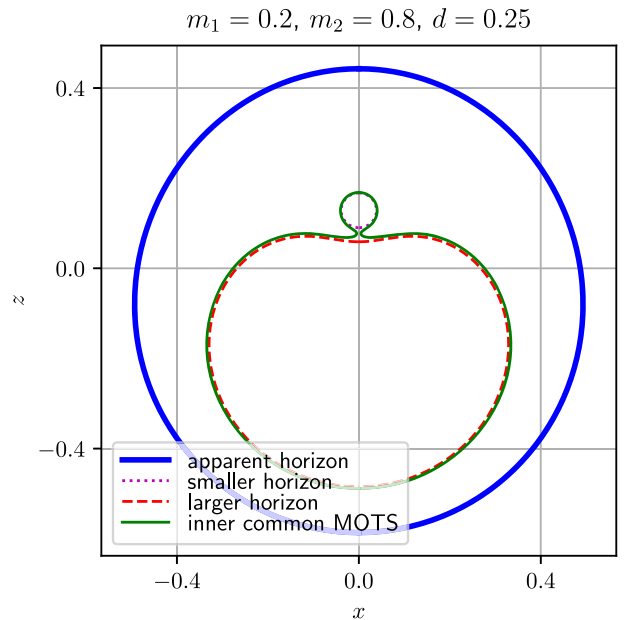


(a) The various marginal surfaces shortly after the common MOTS is formed. For this separation, the inner common MOTS and the AH are very close to each other.

(b) The inner common MOTS and the AH rapidly move away from each other as  $d$  is decreased. The individual MOTSs are relatively undistorted at this stage.



(c) Here  $d$  is further decreased and the inner common MOTS starts getting distorted while the AH becomes more uniform. The larger individual MOTS starts getting distorted as well.



(d) The inner common MOTS and the larger individual MOTS are now highly distorted; the inner common MOTS is clearly not star-shaped. The smaller individual MOTS acts as a barrier and prevents them from merging.

FIG. 1. Sequence for MOTS for BL data. In each of the plots the masses are fixed at  $m_1 = 0.2$ ,  $m_2 = 0.8$ , and the separation  $d$  is successively smaller.

which can exist in a simple binary black-hole initial dataset, namely the Brill-Lindquist (BL) dataset representing non-spinning black holes at a moment of time symmetry. A similar project aimed at studying apparent horizon jumps

was initiated in [39] and also looked at marginal surfaces in a sequence of initial data sets. It was applied to a different initial data construction (Bowen-York); however, only limited results for the equal mass case were presented

there. The MOTS finder used in that work was a pseudo-spectral axisymmetric code using bispherical coordinates and therefore not easily generalizable. See also [55] for a study of distorted horizons in extreme mass ratio systems. See also [56] for another example. Despite the simplicity of BL initial data, we demonstrate the remarkably rich behavior of marginal surfaces, shown here in such great detail for the first time.<sup>1</sup> The MOTSs in BL data do have some special features which we shall mention later. However, as far as the goals of our study are concerned, nothing is lost by restricting ourselves to BL data. Just as for generic initial data, the number of marginal surfaces is the same, and these surfaces are not any less distorted. Furthermore, since numerical accuracy is of paramount importance here, it is more fruitful to initially focus on studying sequences of initial data where additional numerical errors due to time evolution can be ignored. Once the basic link between stability and existence has been established, as will be done in this paper, we can proceed to apply these methods to other initial data and, more importantly, to time evolutions in forthcoming work.

The plan for the rest of this paper is as follows. The basic definitions and mathematical properties of marginally trapped surfaces are given in Sec. II A, and Sec. II B summarizes existing methods for locating marginal surfaces. Section III describes our new method, including the parameterization in Sec. III A, the algorithm in Sec. III B, and its validation in Sec. III C. Section IV provides the first set of results, by applying this method to simple binary black-hole initial data, namely the BL data, representing the head-on collision of two nonspinning black holes initially at rest, considering various values of the mass ratio and various separations. Section V explains many of the results seen in Sec. IV in terms of stability. It shows the crucial link between the existence and stability of marginal surfaces. Finally, the universal behavior of the apparent horizon as  $d \rightarrow 0$  is shown in Sec. VI, and final conclusions are given in Sec. VII.

## II. LOCATING MARGINALLY TRAPPED SURFACES

### A. Definitions and properties

Let  $\mathcal{S}$  be a closed spacelike 2-surface embedded in a spacetime  $\mathcal{M}$  with a Lorentzian metric  $g_{ab}$  of signature  $(-+++)$ . Let  $q_{ab}$  be the Riemannian metric on  $\mathcal{S}$  obtained by restricting  $g_{ab}$  to vectors tangent to  $\mathcal{S}$ . At any point  $p \in \mathcal{S}$ , we can perform an orthogonal decomposition of the tangent space  $T_p\mathcal{M} = T_p\mathcal{S} \oplus T_p\mathcal{S}^\perp$ . The orthogonal space  $T_p\mathcal{S}^\perp$  has a Lorentzian metric, and we can choose a basis of future directed null vectors  $(\ell^a, n^a)$  in this vector space. We assume also that it is possible to assign an *outward* direction on  $\mathcal{S}$ , and by convention  $\ell^a$  is taken to be outward pointing and  $n^a$  inward pointing.

We can in principle rescale  $\ell^a$  and  $n^a$  by positive definite functions; however, it is convenient to tie the scalings of  $(\ell^a, n^a)$  together so that their inner product is preserved:  $\ell \cdot n = -1$ . We are then left with possible rescalings (the boost transformations) such that  $\ell^a \rightarrow f\ell^a$ ,  $n^a \rightarrow f^{-1}n^a$ ,  $f > 0$ .

Let  $\nabla_a$  be the derivative operator on  $\mathcal{M}$  compatible with  $g_{ab}$ . The expansions of  $\ell^a$  and  $n^a$  are, respectively,

$$\Theta_{(\ell)} = q^{ab}\nabla_a\ell_b, \quad \Theta_{(n)} = q^{ab}\nabla_an_b. \quad (1)$$

Under a boost, the expansions scale as  $\Theta_{(\ell)} \rightarrow f\Theta_{(\ell)}$  and  $\Theta_{(n)} \rightarrow f^{-1}\Theta_{(n)}$ .

$\mathcal{S}$  is said to be a marginally outer trapped surface (MOTS, or simply marginal surface) if  $\Theta_{(\ell)} = 0$ . This definition is boost invariant (and invariant under all Lorentz transformations which preserve the direction of  $\ell^a$ ). While we will not generally require any condition on  $\Theta_{(n)}$ , it will be negative in most physical situations, and it is important to check that this is indeed the case. Closed spacelike 2-surfaces with  $\Theta_{(\ell)} = 0$  and  $\Theta_{(n)} < 0$  are called marginally future trapped surfaces. Even in Schwarzschild spacetime, there are examples of nonsymmetric spatial slices which get arbitrarily close to the future singularity but do not contain any marginally trapped surfaces. These slices would have marginal surfaces, i.e., with  $\Theta_{(\ell)} = 0$ , but they would not satisfy  $\Theta_{(n)} < 0$  [57,58].

In the situation of interest for us, namely numerical simulations of Einstein's equations as an initial value problem, the spacetime  $\mathcal{M}$  is foliated by spacelike Cauchy surfaces  $\Sigma_t$  labeled by a real parameter  $t$ . Let  $\mathcal{S}_t$  be a MOTS in  $\Sigma_t$ . Further,  $t^a$  denotes the unit timelike normal to  $\Sigma_t$ ,  $r^a$  the unit spacelike normal to  $\mathcal{S}$  in  $\Sigma_t$ ,  $h_{ab}$  the Riemannian metric on  $\Sigma_t$  induced by  $g_{ab}$ , and  $D_a$  the derivative operator on  $\Sigma_t$  compatible with  $h_{ab}$ . Denote the extrinsic curvature of  $\Sigma_t$  by  $K_{ab} := -h_a^c h_b^d \nabla_c t_d$  (the negative sign is conventional in the numerical relativity literature). A suitable choice of the null normals is

$$\ell^a = \frac{1}{\sqrt{2}}(t^a + r^a), \quad n^a = \frac{1}{\sqrt{2}}(t^a - r^a). \quad (2)$$

Note that for a given  $\mathcal{S}_t$  choosing a different  $\Sigma_t$  corresponds to some boost transformation. The MOTS condition is, as we have seen, boost invariant. Thus, if two hypersurfaces  $\Sigma_t$  and  $\Sigma'_t$  contain  $\mathcal{S}$ , then  $\mathcal{S}$  is a MOTS in both hypersurfaces.

In terms of  $t^a$  and  $r^a$ ,  $\Theta_{(\ell)} = 0$  is equivalent to

$$D_a r^a + K_{ab} r^a r^b - K = 0. \quad (3)$$

This is the equation that must be solved on  $\Sigma_t$ , with given  $K_{ab}$  and  $h_{ab}$ , to locate the MOTS. If we write the MOTS  $\mathcal{S}$  as the level set of some function  $F$ , then  $r_a \propto D_a F$ , and we

<sup>1</sup>Read the previous sentence in David Attenborough's voice.

get a second-order differential equation for  $F$ . We shall write this explicitly below, but for now we conclude this section with a short summary of some properties of MOTSs and the relation between MOTSs and black-hole horizons.

In the context of a time evolution, perhaps the first basic question that arises is whether a given MOTS evolves smoothly. It is *a priori* possible that a MOTS is poorly behaved under time evolution and may arbitrarily cease to exist, or a new MOTS may be formed arbitrarily. In numerical simulations, it is empirically observed that a MOTS does behave smoothly under time evolution. Mathematically this has so far been proven for MOTSs with a physically well-motivated stability condition [46–49]; see also [59] for a study of variations of unstable horizons.

Define first the *variation* of  $\Theta_{(\ell)}$  in the radial direction  $r^a$ ,  $\delta_{fr}\Theta_{(\ell)}$  [60]. Let  $\mathcal{S}_\zeta$  be a smooth one-parameter family of closed spacelike 2-surfaces on  $\Sigma_t$  such that  $\mathcal{S}_{\zeta=0}$  coincides with  $\mathcal{S}$ . Each point  $p$  on  $\mathcal{S}$  traces a smooth curve as  $\zeta$  is varied. Let  $k^a$  be the tangent vector to this curve. On each  $\mathcal{S}_\zeta$  calculate the outgoing null expansion  $\Theta_{(\ell)}^\zeta$  and differentiate it with respect to  $\zeta$ . This yields the variation of  $\Theta_{(\ell)}$  along  $k^a$ :

$$\delta_k \Theta_{(\ell)} := \left. \frac{d\Theta_{(\ell)}^\zeta}{d\zeta} \right|_{\zeta=0}. \quad (4)$$

It is easy to see that the variation is linear for constants but not for a function:  $\delta_{ck}\Theta_{(\ell)} = c\delta_k\Theta_{(\ell)}$  for a constant  $c$ , but  $\delta_{\psi k}\Theta_{(\ell)} \neq \psi\delta_k\Theta_{(\ell)}$  when  $\psi$  is a nonconstant function.

Choose  $k^a = fr^a$ , and define the operator  $L$  as

$$\delta_{fr}\Theta_{(\ell)} =: Lf. \quad (5)$$

It can be shown that  $L$  is generally of the form

$$Lf = -\Delta f + \gamma^a \partial_a f + \beta f, \quad (6)$$

where  $\Delta$  is the Laplacian compatible with  $q_{ab}$ ,  $\gamma^a$  is some vector field on  $\mathcal{S}$  (related to the angular momentum) and  $\beta$  is a scalar. In the case of time-symmetric data (where the angular momentum and hence  $\gamma^a$  vanishes), the stability operator can be simplified to [47]

$$Lf = -\Delta f - (R_{ab}r^a r^b + \mathcal{K}_{ab}\mathcal{K}^{ab})f. \quad (7)$$

Here  $R_{ab}$  is the intrinsic Ricci tensor of  $\Sigma_t$ , and  $\mathcal{K}_{ab}$  is the second fundamental form of  $\mathcal{S}$  embedded in  $\Sigma_t$ . In this case  $L$  is seen to be self-adjoint.

In general however, from Eq. (6),  $L$  is a second-order elliptic operator with a discrete spectrum, which is however not necessarily self-adjoint. Its smallest eigenvalue, known as the principal eigenvalue  $\Lambda_0$ , turns out to be real. It was shown that if the principal eigenvalue is positive, then the MOTS evolves smoothly in time [46–48]. This stability

condition is equivalent to saying that an outward deformation of  $\mathcal{S}$  makes it untrapped, which is what we expect to happen for the apparent horizon. We shall study the stability operator and its first eigenvalues below in much greater detail in specific examples.

In the introduction, we mentioned briefly the idea of stacking up marginal surfaces at different times to construct a smooth 3-surface, a quasilocal horizon. The only notion from the formalism of quasilocal horizons that we will use in this paper is that of mass multipole moments. Given a 2-sphere  $\mathcal{S}$  with an axial symmetry vector  $\phi^a$  and an intrinsic Ricci scalar  $\mathcal{R}$ , it turns out to be possible to construct a set of geometric multipole moments which capture the intrinsic horizon geometry [61]. Since we shall deal with time-symmetric situations, we do not need to consider the current multipole moments and we restrict ourselves to the mass multipoles  $I_n$ . These are

$$I_n = \sqrt{\frac{2n+1}{4\pi}} \int_{\mathcal{S}} \mathcal{R} P_n(\zeta) d^2V \quad (8)$$

with the coordinate  $\zeta \in [-1, 1]$  (the analog of  $\cos\theta$  in standard spherical coordinates) defined as

$$\partial_a \zeta = \frac{1}{R^2} \epsilon_{ba} \phi^b, \quad \int_{\mathcal{S}} \zeta d^2V = 0. \quad (9)$$

Here  $R$  is the radius of  $\mathcal{S}$ ,  $\epsilon$  the volume 2-form on  $\mathcal{S}$ , and  $P_n$  the  $n$ th Legendre polynomial.

## B. Locating star-shaped MOTSs numerically

Most MOTS finders assume, first of all, that the 2-surface  $\mathcal{S}$  is topologically a sphere. This is not a strong restriction as it can be shown that generically the topology must be spherical, it is toroidal only in very special situations, and higher genus surfaces are not allowed [62]. The other common assumption is that  $\mathcal{S}$  demarcates a star-shaped region (Strahlkörper); i.e., any ray drawn from the origin intersects  $\mathcal{S}$  exactly once. This is obviously a coordinate-dependent definition since it depends on the origin and on the set of coordinates in which straight lines are drawn. It excludes surfaces of the form shown in Fig. 1.1 of [52], and we shall show explicit examples of non-star-shaped surfaces very much like it [e.g., Fig. 1(d)]. Given this assumption, we can parameterize  $\mathcal{S}$  as

$$r = h(\theta, \phi), \quad (10)$$

where  $r$  is the Euclidean distance from the origin of coordinates to a point on  $\mathcal{S}$  and  $(\theta, \phi)$  are angular coordinates. Here  $(r, \theta, \phi)$  is the coordinate system used in the numerical calculations, and we shall use mid-alphabet Latin indices  $i, j, \dots$  for tensors in this coordinate system. Thus,  $h_{ij}$  is a Riemannian metric [not to be confused with  $h(\theta, \phi)$ ] and  $K_{ij}$  the extrinsic curvature.

We look for level sets of the function

$$F(r, \theta, \phi) = r - h(\theta, \phi). \quad (11)$$

The surfaces of constant  $F$  define a sequence of surfaces and, to compute the normal, we start with the gradient of  $F$ :

$$s_i = \partial_i F, \quad dF = dr - h_\theta d\theta - h_\phi d\phi. \quad (12)$$

The unit-normal  $r_i$  is then

$$r_i = \frac{s_i}{\|s\|}, \quad \|s\|^2 = h^{ij} s_i s_j. \quad (13)$$

Since  $s_i$  is directly related to the derivative of  $h(\theta, \phi)$ , as opposed to  $r_i$  which has a complicated nonlinear dependence, it is convenient to separate out the norm of  $s_i$  in the expansion.

Since  $r^i$  is proportional to  $\|s\|^{-1}$ , looking at the three terms in Eq. (3), we see immediately that  $K_{ij} r^i r^j$  is proportional to  $\|s\|^{-2}$  and  $K$  does not depend on  $\|s\|$ . In the first term  $D_i r^i$ , since  $r^i$  is proportional to  $\|s\|^{-1}$ , it is clear that differentiation will lead to two terms, one proportional to  $\|s\|^{-3}$  and the other to  $\|s\|^{-1}$ :

$$D_i \left( \frac{s^i}{\sqrt{s \cdot s}} \right) = \frac{D_i s^i}{(s \cdot s)^{1/2}} - \frac{s^i s^j D_i s_j}{(s \cdot s)^{3/2}}. \quad (14)$$

Thus, the expansion of any level-set surface of  $F$  is of the form

$$\Theta = \frac{A}{\|s\|^3} + \frac{B}{\|s\|} + \frac{K_{ij} s^i s^j}{\|s\|^2} - K, \quad (15)$$

where

$$A := -s^i s^j \partial_i s_j - \frac{1}{2} s^i (\partial_i h^{kl}) s_k s_l, \quad (16a)$$

$$B := (\partial_i h^{ij}) s_j + h^{ij} \partial_i s_j + (\partial_i \ln \sqrt{\det[h]}) s^i. \quad (16b)$$

Here  $\det[h]$  is the determinant of  $h_{ij}$ . In terms of the function  $h$  we are trying to solve for,  $\Theta_{(\ell)}$  depends on  $h$  and its first two derivatives. We thus end up with a second-order nonlinear elliptic partial differential equation for  $h$  whose coefficients depend on  $h_{ij}$ , its first derivatives, and  $K_{ij}$ .

The method using the above formalism, with the assumption of a star-shaped surface, i.e., using Eq. (11), and following the implementation of [15] is routinely used in numerical simulations. While this is generally sufficient for many applications, there are cases where highly distorted MOTSs appear. An example is in [28], where certain highly distorted MOTSs appear and this standard approach does not work. We will see that this restriction can be

removed by a small change while still leaving most aspects of the above approach intact.

### III. LOCATING A DISTORTED MOTS

We begin by reinterpreting the starting point of the algorithm, i.e., Eq. (11). Instead of the radial distance  $r$  from the origin, we could choose to use the distance from a sphere of some radius  $R_0$  along rays orthogonal to the sphere<sup>2</sup> (the precise radius of the sphere is not important). Since the rays emanating from the sphere in the orthogonal direction all meet at the origin, the two interpretations are identical and the numerical method and results are unchanged. The restriction to a star-shaped surface obviously still holds. However, we are free to take as reference a topologically spherical surface of any arbitrary shape and we can consider rays orthogonal to it. The rays will now not necessarily all meet at the origin (or at any other point), but this is irrelevant. What is important is that the reference surface can be chosen so that the rays orthogonal to it meet the surface  $\mathcal{S}$  just once. The reference surface itself need not be star shaped either; it just needs to be parameterized suitably, as we shall discuss later. Furthermore, it is important that the rays do not intersect each other *before* reaching  $\mathcal{S}$ . This typically happens when  $\mathcal{S}$  is too far away from the reference surface; it is beyond the region of validity of this coordinate system based on the reference surface.

An example of the numerical benefits of choosing a suitable reference surface is shown in Fig. 2. The surface  $\mathcal{S}$  is the MOTS that we are trying to locate. The first panel of Fig. 2 is the standard method, i.e., using rays centered at the horizon. The surface  $\mathcal{S}$  is of the type that is difficult to locate and comes close to, or even violates, the property of being star shaped; this is very similar to Fig. 1.1 of [52] shown there as an example of a problematic surface. In Fig. 2, the surface  $\mathcal{S}$  is actually star shaped, but only barely. We see that the rays centered at the origin intersect  $\mathcal{S}$  only once, but the intersections pile up at the neck. On the other hand, the second panel shows a reference surface  $\sigma_R$  which is only slightly deformed away from an exact sphere. The rays are now orthogonal to  $\sigma_R$  and we see that the intersections are much more uniformly distributed on  $\mathcal{S}$ . While it is clearly possible to find reference surfaces which make it harder to locate  $\mathcal{S}$ , there are many easily found choices which greatly improve the numerical results. This also makes the algorithm very flexible, as it can be tuned to find extremely distorted surfaces.

<sup>2</sup>Here orthogonality refers just to a Euclidean metric in the coordinate system where the numerical calculations are being performed. Similarly straight lines refer to this fictitious Euclidean metric and not to geodesics of the physical Riemannian metric.

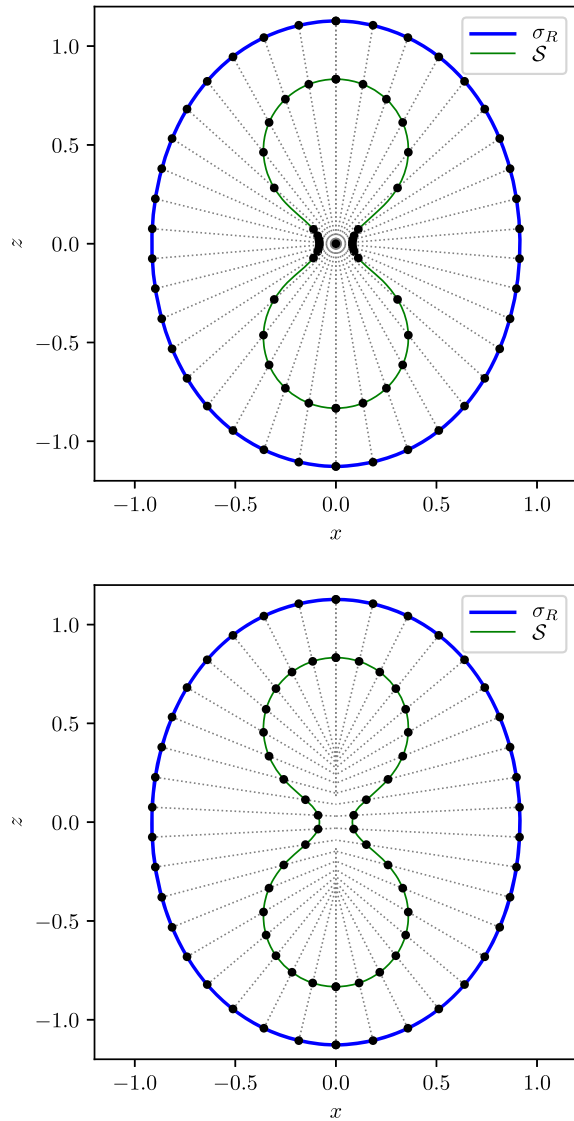


FIG. 2. This figure shows the benefits of using a nonspherical reference surface. The surface  $S$  in both panels is the MOTS we are trying to locate; it is star shaped, but only barely so. The first panel is the standard approach using rays centered at the origin while the second panel uses rays orthogonal to a reference surface  $\sigma_R$ . See text for further discussion.

### A. The new coordinate system

Consider then a reference surface  $\sigma_R$  parameterized by two coordinates  $(\lambda_1, \lambda_2)$  (the generalization to greater or fewer dimensions is obvious). The parameters  $(\lambda_1, \lambda_2)$  could be for example angular coordinates  $(\theta, \phi)$  but this is not a requirement. Construct then the rays orthogonal to  $\sigma_R$  using the Euclidean metric in which the numerical simulation is being carried out. To any point in the neighborhood of  $\sigma_R$ , we can assign coordinates  $(\xi, \lambda_1, \lambda_2)$ , where  $\xi$  is the Euclidean distance along the orthogonal rays; see Fig. 3. This coordinate system is valid as long as the orthogonal rays do not cross. This construction is very similar to Gaussian or Fermi-normal coordinates in

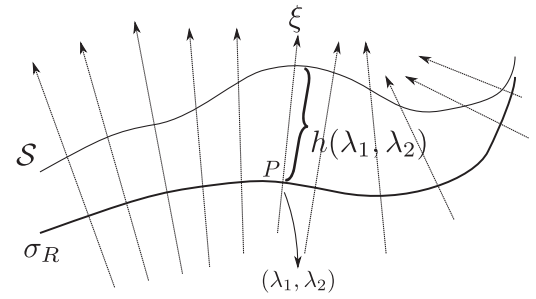


FIG. 3. The coordinate system  $(\xi, \lambda_1, \lambda_2)$  based on a reference surface  $\sigma_R$  and the rays orthogonal to it.  $\xi$  is the Euclidean distance along the orthogonal rays and  $(\lambda_1, \lambda_2)$  are the coordinates of the point  $P$  which is the intersection of the ray and  $\sigma_R$ . The surface  $S$  we are looking for can be represented by a height function  $h$ .

differential geometry, except that we do not use the actual curved geometry to define the orthogonal rays, nor do we use the proper distance along the rays.

Given the coordinate system  $(\xi, \lambda_1, \lambda_2)$ , we can represent the surface  $S$  that we are looking for by a height function  $h$ . Then, analogous to Eq. (11), we want to consider level sets of the function

$$F(\xi, \lambda_1, \lambda_2) = \xi - h(\lambda_1, \lambda_2). \quad (17)$$

The normal to  $S$  is again the gradient of  $F$ :  $s_i = \partial_i F$ . Obviously,  $(\xi, \lambda_1, \lambda_2)$  must be known as functions of the coordinates used in the simulation. The important point is that Eq. (15) still remains valid. The difference now is that, instead of Eq. (11), we use Eq. (17) to define the normal  $s_i$ . The numerical method for solving the equation is not affected by this parameterization.

While it should be clear that the method should work generally, in the rest of this paper, we shall restrict ourselves to the axisymmetric case where we only need to consider reference curves parameterized by a single parameter  $\lambda$ . The validation of the code and results for the general three-dimensional case will be left to future work. Let the symmetry axis be the  $z$  axis, and let us work in the  $x-z$  plane. We represent a reference surface  $\sigma_R$  via a parameterized curve which we shall denote  $\gamma_R(\lambda)$ . We are free to choose the parameter  $\lambda$  as convenient. For example we could take it to be the angle with the  $z$  axis—but this would restrict us to take the reference surface as star shaped. More generally, we could take it to be the path length of the curve. Whatever the choice, we shall take the range of the parameters to be from 0 to  $\pi$ . Thus we have a curve  $\gamma_R: [0, \pi] \rightarrow \mathbb{R}^2$  in the  $x-z$ -coordinate plane such that  $\gamma_R(0)$  and  $\gamma_R(\pi)$  lie on the  $z$  axis and the tangent vectors  $\gamma'_R(0)$  and  $\gamma'_R(\pi)$  are perpendicular to the  $z$  axis.

Let  $\vec{x}$  be the vector representing any point in the  $x-z$  plane; we remind the reader again that the simulations are in Euclidean coordinates. We define

$$F(\vec{x}) := \xi(\vec{x}) - h(\lambda(\vec{x})), \quad (18)$$

where  $\xi(\vec{x})$  and  $\lambda(\vec{x})$  are defined implicitly by

$$\vec{x}(\xi, \lambda) = \vec{\gamma}_R(\lambda) + \xi \vec{\nu}_R(\lambda). \quad (19)$$

Here  $\vec{\nu}_R$  is a vector pointing outwards in the direction normal to  $\sigma_R$  in the (Euclidean)  $x, z$  coordinates. Note that we do not require  $\vec{\nu}_R$  to be normalized to unit length. This will make the computational tasks much easier, since it allows us to simply choose  $\nu_R$  to be the tangent vector rotated by  $\pi/2$ .

Using this ansatz, the horizon function  $h$  defines the surface  $\mathcal{S}$  (for which  $F = 0$ ) via the curve

$$\vec{\gamma}(\lambda) = \vec{\gamma}_R(\lambda) + h(\lambda)\vec{\nu}_R(\lambda). \quad (20)$$

As before, taking the normal  $s_i$  to this curve and using it in Eq. (15) yields the differential equation that we need to solve.

## B. The numerical algorithm

As discussed above, the equation to solve numerically is (15) with our definition of  $F$  from Eq. (18) used to define the normal  $s_i$ . This is then read as a nonlinear partial differential equation (PDE) for  $h$ , which becomes a nonlinear ordinary differential equation in axisymmetry. Our method of solving this equation is standard Newton root finding, suitably extended to differential operators via the Newton-Kantorovich scheme [63]. Other means of solving the nonlinear PDE, e.g., [52], can also be used. Let  $\mathcal{N}$  be the differential operator so that the equation to be solved is  $\mathcal{N}(u) = 0$ . We will need the variational derivative  $\mathcal{N}_u$  of  $\mathcal{N}(u)$  defined in the usual manner:

$$\mathcal{N}_u(\Delta) = \lim_{\epsilon \rightarrow 0} \frac{\mathcal{N}(u + \epsilon\Delta) - \mathcal{N}(u)}{\epsilon}. \quad (21)$$

Here  $\Delta$  is a variation of  $u$  and  $\mathcal{N}_u$  is a differential operator (obtained by linearizing  $\mathcal{N}$ ) acting on  $\Delta$ .

Start with an initial guess  $u^{(0)}$ , and let  $u^{(i)}$  be the  $i$ th iteration. If this is sufficiently close to the true solution, we can expand  $\mathcal{N}(u)$  linearly around  $u^{(i)}$  to obtain

$$0 = \mathcal{N}(u^{(i)} + \Delta) \approx \mathcal{N}(u^{(i)}) + \mathcal{N}_u \Delta. \quad (22)$$

We want to choose  $u^{(i+1)}$  by solving the linear system of equations

$$u^{(i+1)} = u^{(i)} - \mathcal{N}_u^{-1} \mathcal{N}(u^{(i)}); \quad (23)$$

i.e., we solve  $\mathcal{N}_u \Delta = -\mathcal{N}(u^{(i)})$  for  $\Delta$  (with suitable boundary conditions to be detailed below) and perform

the steps  $u^{(i+1)} = u^{(i)} + \Delta$ . This applies whether  $u$  is represented by values on a discrete grid or as spectral coefficients.

Our implementation uses a pseudospectral method [63,64] to perform the steps (23), where  $u^{(i)}(\lambda) = h^{(i)}(\lambda)$  and  $\mathcal{N}(u) = \Theta(h)$  as defined in (15). The linear equation for  $\Delta$  now takes the form

$$(\delta_h \Theta) \Delta + (\delta_{h'} \Theta) \Delta' + (\delta_{h''} \Theta) \Delta'' = -\Theta(h^{(i)}). \quad (24)$$

Here, the derivatives of  $\Theta$  on the left-hand side of (24) are evaluated at  $h^{(i)}$ . Note that, in each step,  $h^{(i)}$  defines a *trial surface*  $\mathcal{S}^{(i)}$  which is tested for convergence by computing its expansion  $\Theta$  at a finite set of points.

To apply the pseudospectral method, we start with a choice for  $h^{(0)}$ , say  $h^{(0)} \equiv 0$ , and represent  $\Delta$  using a truncated series of cosines:

$$\Delta(\lambda) = \sum_{n=0}^N a_n \cos(n\lambda), \quad (25)$$

where we call  $N$  the *resolution* of a particular pseudospectral representation. This choice of basis functions is natural for the axisymmetric setting and ensures that, for a reference curve  $\gamma_R$  satisfying  $\gamma'_R(0) = \gamma'_R(\pi) = 0$ , the curve represented by  $h$  using (20) does so too. In addition, it eliminates the need to impose explicit boundary conditions when solving the differential equation since this is already done by each individual basis function.

## C. Validating the numerical method

Since the full procedure combines several methods [computation of the variational derivatives in (24), the Newton-like root search, the pseudospectral method], each introducing numerical errors, one possibility for testing the procedure as a whole is to perform the whole search for  $\mathcal{S}$  at different fixed spectral resolutions  $N$  of the steps  $h^{(i)}$ . At each resolution, we compute the maximum  $\|\Theta\|_\infty$  and plot the result as a function of  $N$  in Fig. 4, for a static initial data configuration of two black holes (as described in Sec. IV). The exponential convergence is expected for a spectral method [63] and also shows convergence of the Newton-Kantorovich scheme until the floating point round-off plateau is reached.

The remaining quantity to be tested is the expansion as computed for a (trial) surface  $\mathcal{S}$ . This can be accomplished by comparing the computed expansion with a case where it is known analytically. One of the simplest of such cases is a centered sphere in a Schwarzschild slice  $h_{ab} = \phi^4 \delta_{ab}$ , where

$$\phi(\vec{r}) = \phi(r) = 1 + \frac{m}{2r}. \quad (26)$$

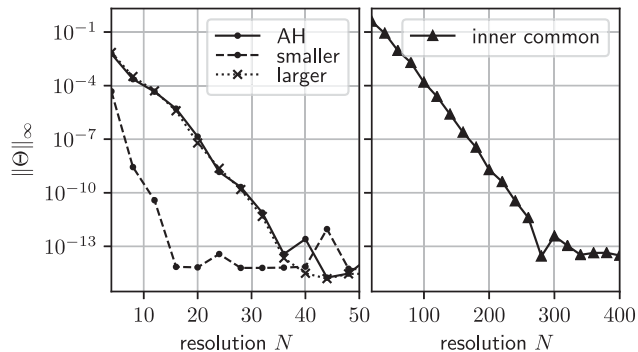


FIG. 4. Convergence of the expansion using results of searches with different spectral resolutions  $N$  for the series representation of  $h^{(i)}$ . The quantity  $\|\Theta\|_\infty$  is computed taking an initial grid with higher density than the resolution  $N$  and performing a local maximum search from the point of largest deviation from zero. The left panel shows the convergence of the outermost common (apparent) horizon and the two individual MOTSs, while the right panel shows the convergence for the inner common MOTS which has a more distorted shape and hence requires a higher resolution. The expected exponential falloff continues until the floating point roundoff plateau is reached. As can be seen, this happens at different resolutions depending on the specific form of the respective surface  $\mathcal{S}$  and the reference surface  $\sigma_R$ . The configuration used here is that of Fig. 1(c) with reference surfaces taken as the respective horizons for  $d = 0.405$ .

The expansion of  $r = \text{const}$  surfaces is then given by

$$\Theta = \frac{2}{\phi^2(r)} \left( \frac{1}{r} + 2 \frac{\phi'(r)}{\phi(r)} \right). \quad (27)$$

Figure 5 shows that the numerically computed expansion agrees to high accuracy with the exact value. The event horizon and apparent horizon coincide in these slices and are located at  $r = m/2$  in these coordinates. A respective search with a reference surface chosen to be  $r = m = 1$  converges to a curve  $\gamma$  with  $|\gamma(\lambda)| = m/2 \pm 5 \times 10^{-17}$  and a numerically evaluated expansion  $\|\Theta\|_\infty \lesssim 10^{-15}$ .

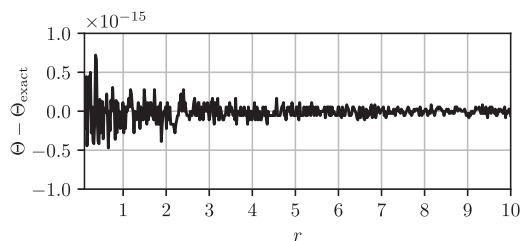


FIG. 5. Accuracy of the expansion computed for an  $r = \text{const}$  surface in a Schwarzschild slice with mass  $m = 1$ . The reference surface  $\sigma_R$  is here chosen to be a sphere of radius  $r/2$ .

## IV. APPLICATION TO TIME-SYMMETRIC BINARY BLACK-HOLE INITIAL DATA

### A. Brill-Lindquist initial data

We apply our new MOTS finder algorithm to the Brill-Lindquist (BL) initial dataset. This is perhaps the simplest initial dataset [65] representing multiple nonspinning black holes at a moment of time symmetry. Thus, each black hole has vanishing momentum. The original work [65] considered also electric charge and an arbitrary number of black holes, but here we shall ignore charge and restrict ourselves to two black holes. While simple, this initial dataset is not simplified in terms of the various kinds of MOTSs that can appear. As shown numerous times in the literature, (see e.g., [28]), the general picture is that, when the two black holes in the binary are initially well separated, there are two independent MOTSs, one for each black hole. These two MOTSs approach each other and, at a certain point, a common MOTS appears which surrounds the individual MOTSs. This common MOTS immediately bifurcates into an inner and outer MOTS. The inner common MOTS shrinks and approaches the two individual MOTSs, while the outer common MOTS (the apparent horizon) grows and sheds its multipole moments to approach an equilibrium state, i.e., a Kerr black hole.<sup>3</sup> The eventual fate of the inner MOTS and the two individual MOTSs is still unknown, though some partial results are known [28,66].

Time symmetry means that the extrinsic curvature vanishes:  $K_{ab} = 0$ . The 3-metric is conformally flat:  $h_{ab} = \phi^4 \delta_{ab}$ . The two black holes are represented by two punctures in the background conformal metric  $\delta_{ab}$ . The Euclidean distance between the punctures is  $d$  and the conformal factor at any point  $\vec{r}$  is

$$\phi(\vec{r}) = 1 + \frac{m_1}{2r_1} + \frac{m_2}{2r_2}. \quad (28)$$

Here  $r_1$  and  $r_2$  are the Euclidean distances of  $\vec{r}$  from the two punctures and  $m_1$  and  $m_2$  are the bare masses of the two black holes. As shown in [65], the total Arnowitt-Deser-Misner (ADM) mass of the system is  $M_{ADM} = m_1 + m_2$ . The two punctures are regular asymptotic ends, and ADM masses can thus be calculated at the punctures:

$$M_{ADM}^{(1)} = m_1 + \frac{m_1 m_2}{2d}, \quad (29)$$

$$M_{ADM}^{(2)} = m_2 + \frac{m_1 m_2}{2d}. \quad (30)$$

The difference

$$M_{ADM} - M_{ADM}^{(1)} - M_{ADM}^{(2)} = -\frac{m_1 m_2}{d} \quad (31)$$

<sup>3</sup>Or, in our simplified case of axial symmetry and no spins, a Schwarzschild black hole.

is interpreted as the binding energy. For nonspinning black holes, the irreducible mass, i.e.,  $M_{\text{irr}} = \sqrt{A/16\pi}$  with  $A$  being the area of the MOTS, provides an appropriate notion of horizon mass. The difference between the bare masses and the horizon masses ( $M_{\text{ADM}} - M_{\text{irr}}^{(1)} - M_{\text{irr}}^{(2)}$ ) is interpreted similarly, yields similar results, is applicable for a much wider variety of initial data, and is in fact physically more meaningful [27,67].

The qualitative structure of the MOTSs described above as arising from time evolution is also present when the static distance  $d$  is reduced. As far as the various MOTSs are concerned, there is no reduction in complexity by simplifying the initial data. The main difference is that for time-symmetric data a MOTS is also a surface of extremal area (boosted Bowen-York data, in which MOTSs are not extremal, were used to explore this point in [39]). As in time evolution, and as shall be shown below, all of the individual and the inner and outer MOTSs are present. As  $d$  becomes smaller, the inner common MOTS becomes highly distorted and extant horizon finders have not been able to find it. With our new numerical method, we shall be able to track this inner MOTS even as it becomes highly distorted and eventually disappears. It should be kept in mind however that changing  $d$  alone is not equivalent to time evolution and quantitative results may not carry through to a real time evolution. In a real time evolution the data will not remain time symmetric. Also, decreasing  $d$  alone keeps the total ADM mass fixed but leads to increasing  $M_{\text{ADM}}^{(1,2)}$  as is obvious from the above equations. A true time evolution will, in principle, keep all ADM masses fixed.

## B. Results: Distorted MOTSs in BL data

We can now begin with our main results, namely properties of marginal surfaces in BL data for various values of the masses  $m_{1,2}$  and separations  $d$ . By convention, we shall take  $m_1 \leq m_2$  and the mass ratio is defined as  $q = m_2/m_1 \geq 1$ . The total mass will be kept fixed to unity:  $M = m_1 + m_2 = 1$ . For any given mass ratio, we generally successively decrease the value of  $d$  in the results below. Once we have found a MOTS for a particular  $d$ , it is used as a reference surface for the next smaller value of  $d$ . We have already seen that there are generally four different marginal surfaces. Whenever convenient, the apparent horizon will be denoted  $\mathcal{S}_{\text{AH}}$ , the inner horizon by  $\mathcal{S}_{\text{in}}$ , the larger individual MOTS by  $\mathcal{S}_{\text{large}}$  and the smaller individual MOTS by  $\mathcal{S}_{\text{small}}$ . Obviously for the equal mass case both  $\mathcal{S}_{\text{large}}$  and  $\mathcal{S}_{\text{small}}$  have the same size and the distinction between them will be irrelevant.

### 1. The various MOTSs for mass ratio 1:4

The first set of plots shows the various MOTSs for BL data with a mass ratio 1:4, chosen as an illustrative example. This value of the mass ratio is also the one used

in [66] as an example, and we shall reproduce and extend the results shown in Fig. 2 of [66].

Since the total mass is normalized to unity, the individual masses are  $m_1 = 0.2$  and  $m_2 = 0.8$ . Note that, since the data is time symmetric, the MOTSs are all minimal surfaces and thus they cannot touch each other with a common tangent vector (otherwise, by the maximum principle for elliptic operators, they must coincide [66]). The common horizon is seen to exist for  $d \leq 0.6987162$ .<sup>4</sup> For larger separations we only have the two individual horizons. Figures 1 and 6 show the horizons for  $d = 0.69850, 0.6500, 0.4000, 0.2500, 0.166052351$ . This last value is a little before the inner common MOTS ceases to exist. The last panel [Fig. 6(b)] shows the detailed picture near the neck of the MOTS. It is clear that the inner common MOTS is far from star shaped at this point (in fact this happens much earlier for larger  $d$ ), yet our new horizon finder has no fundamental difficulty in locating it.

For each of the MOTSs, we also look for surfaces of constant expansion [16,69] on both sides. We confirm that indeed the behavior of the apparent horizon is as expected: the expansion goes smoothly from negative to positive values as we cross the apparent horizon going outwards. This is *not* the case for the inner MOTS. The constant expansion surfaces lie on both sides of the MOTS and thus they do not form a regular foliation in any neighborhood of the MOTS; see Fig. 7. This is consistent with the fact that, as we shall see below, the inner MOTS (unlike the apparent horizon) is unstable in the sense discussed in Sec. II A and it thus is not guaranteed to be a barrier between trapped and untrapped surfaces in any neighborhood [46].

As we decrease  $d$ , we observe that the inner common MOTS is not found for  $d < 0.166052351$ , and shortly after that, for  $d < 0.16461385$  the larger individual MOTS is not found as well. For all smaller values of  $d$ , the smaller individual horizon and the apparent horizon continue to exist; the apparent horizon becomes smoother just as in a time evolution [28]. The remaining inner MOTS corresponding to the smaller black hole becomes smaller in coordinate space. We briefly summarize the properties of the 1:4 configuration as  $d$  is decreased.

*Large  $d$ .*—Only  $\mathcal{S}_{\text{large}}$  and  $\mathcal{S}_{\text{small}}$  exist.

$d \approx 0.6987$ .—Common horizon appears and bifurcates into  $\mathcal{S}_{\text{AH}}$  and  $\mathcal{S}_{\text{in}}$ .

$d \lesssim 0.6987$ .— $\mathcal{S}_{\text{in}}$  becomes increasingly distorted.

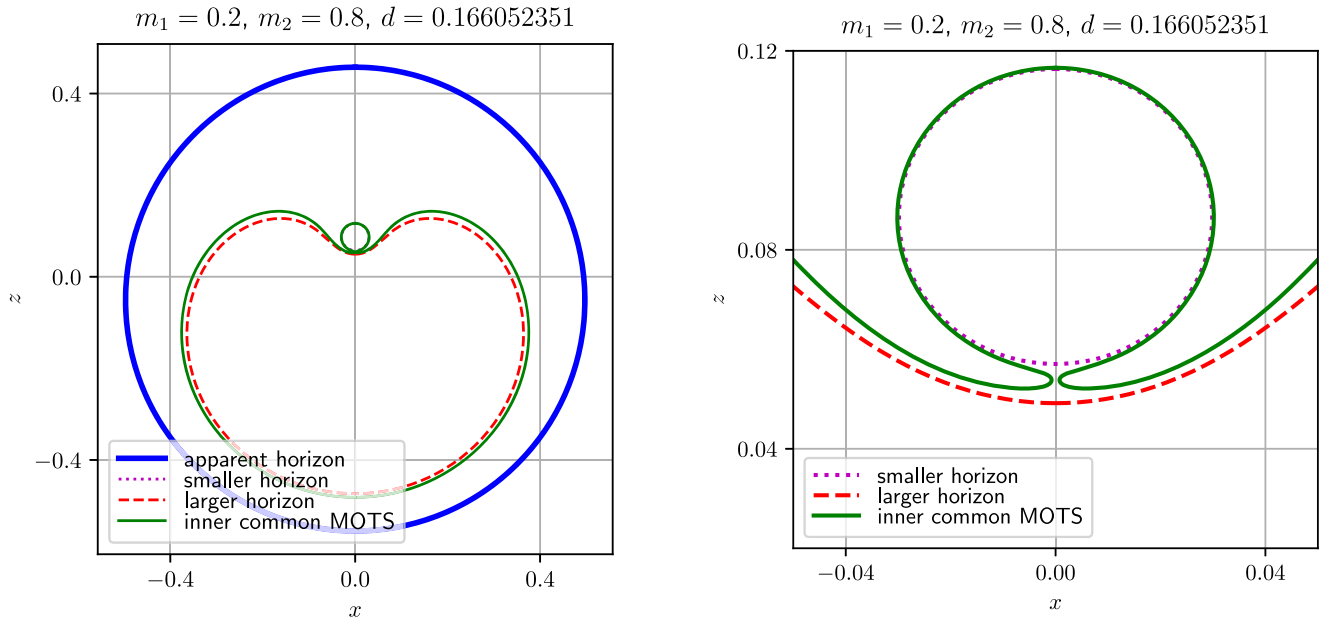
$d \lesssim 0.1660$ .— $\mathcal{S}_{\text{in}}$  no longer found.

$d \lesssim 0.1646$ .— $\mathcal{S}_{\text{large}}$  no longer found.

*Small  $d$ .*—Only  $\mathcal{S}_{\text{AH}}$  and  $\mathcal{S}_{\text{small}}$  exist.

In previous work, say [28], when the inner horizon was not found, it was reasonable to suspect that the numerical method being used there was not able to find it. Here, we

<sup>4</sup>We remark that for the equal mass case we find the common horizon for  $d \leq 0.76619742$ , which agrees within our final step size  $\Delta d = 10^{-8}$  with the results found in [68].



(a) The marginal surfaces just before the extremely distorted inner common MOTS disappears entirely

(b) Detailed view of the inner MOTS at its neck - where it almost seems to be pinching off - just before it disappears.

FIG. 6. The same as Fig. 1 above, but for the smallest value of  $d$  before the inner common MOTS disappears. The right panel (b) shows the details of the highly distorted inner MOTS at its neck.

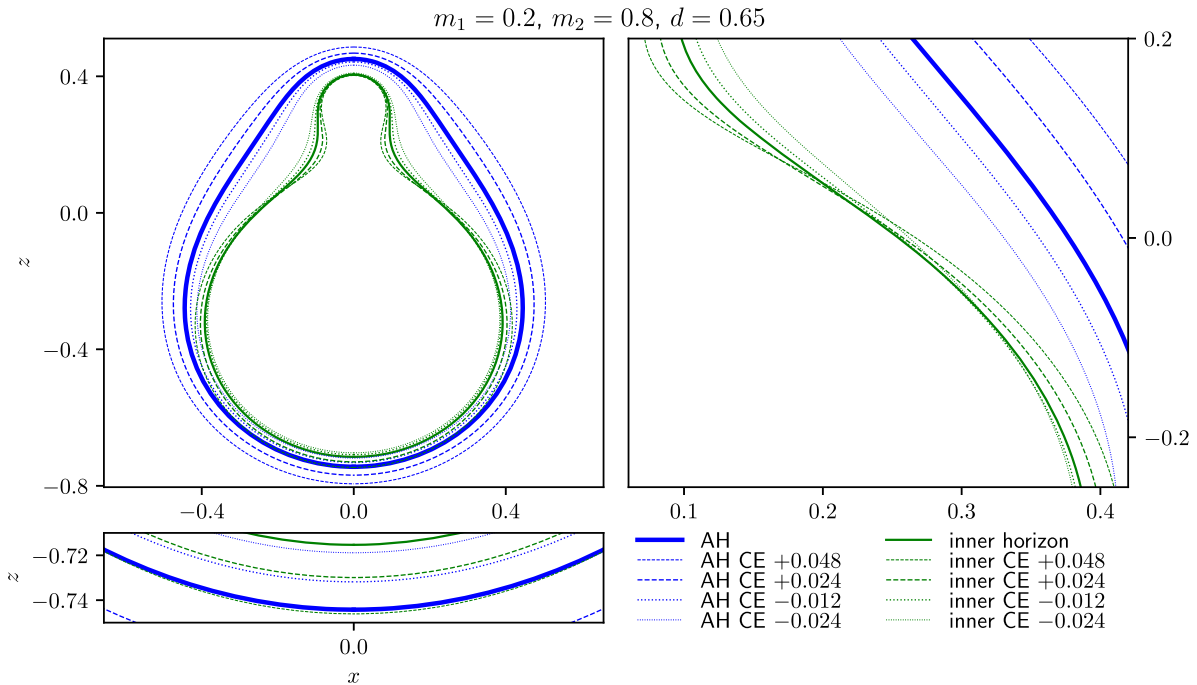


FIG. 7. The constant expansion surfaces near the apparent horizon and the inner common MOTS. This shows that the apparent horizon is stable while the inner MOTS is not. See text for discussion. The right panel shows a close-up of the intersection of surfaces of constant positive and negative expansion with the inner MOTS. The bottom panel shows that the constant expansion surfaces and MOTSs do not coincide and, even though being close, they have different curvatures leading to different expansion values.

have evidence that the inner horizon in fact does not exist. While it is difficult to prove nonexistence with absolute certainty here, we can eliminate a few clear possibilities.

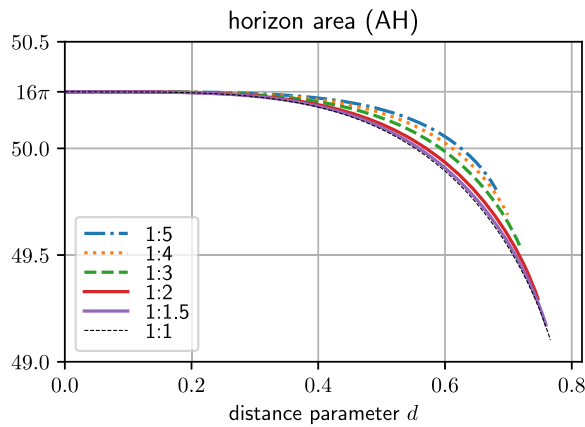
First, we note that, at the point before the MOTS disappears, there is no indication of any numerical problems at the earlier step (in this case for a slightly larger value of  $d$ ). It is true that resolving the neck requires higher resolution, but this is feasible with modern computers. Note also that the larger individual MOTS disappears as well and it does not have any such features that need to be resolved. Second, the foliation by the constant expansion surfaces, in the region near where the inner MOTS is found just before it disappears, shows only negative values of the expansion:  $\Theta_{(\ell)} < c$ , where  $c$  is some nonzero negative number. Just before the MOTS disappears,  $c$  is positive and decreases

to 0 when the last instance of the MOTS is found. This shall be further discussed below in more detail.

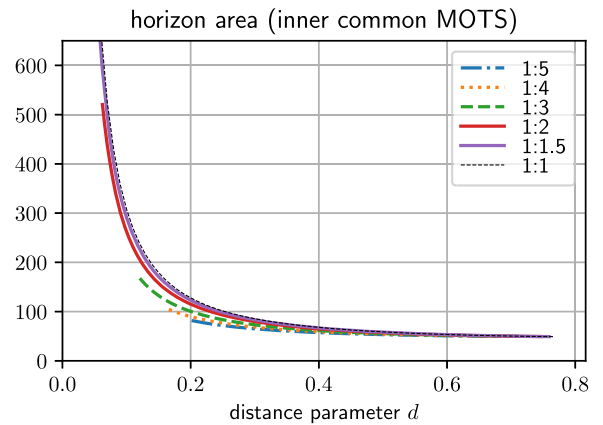
## 2. Varying the mass ratio

We next investigate a number of geometric quantities on the various MOTSs as functions of  $d$  and for different mass ratios. In these results, we consider the mass ratios 1:1, 1:1.5, 1:2, 1:3, 1:4 and 1:5. As before the total mass is always kept fixed:  $M_{\text{ADM}} = m_1 + m_2 = 1$ .

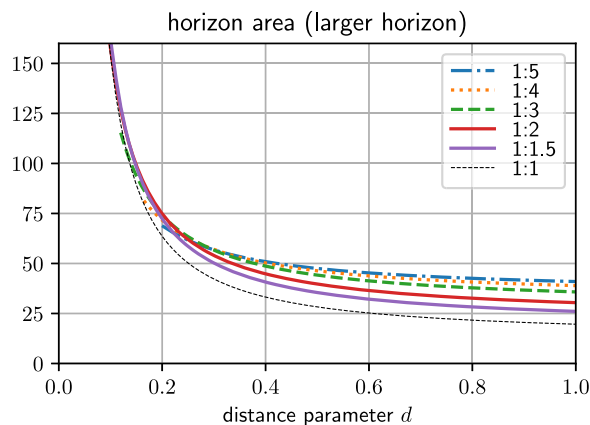
Figure 8 shows the areas of the four horizons as functions of  $d$ . The apparent horizon is the easiest to understand in terms of the irreducible mass  $M_{\text{irr}} = \sqrt{\text{Area}/16\pi}$ . Since the black holes have zero angular momentum,  $M_{\text{irr}}$  is also the correct mass that one should assign to the black hole [26]. As discussed earlier (see also [27]), the difference  $M_{\text{ADM}} - M_{\text{irr}}$



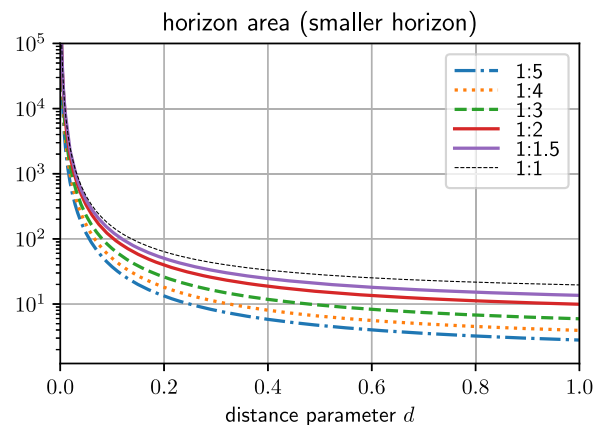
(a) The area of the AH as a function of  $d$  for different mass ratios. As discussed in the text, we get  $16\pi$  as  $d \rightarrow 0$ .



(b) The area of the inner MOTS as a function of  $d$  for different mass ratios, for all values of  $d$  for which the MOTS exists. For smaller mass ratios the MOTS continues existing for smaller  $d$ .



(c) The area of the larger individual MOTS as a function of  $d$  for different mass ratios. As shown in the text, for large  $d$ , the area approaches  $16\pi q^2/(1+q)^2$ , i.e. becomes larger for more asymmetric systems.



(d) The area of the smaller individual MOTS as a function of  $d$  for different mass ratios. As shown in the text, for large  $d$ , the area approaches  $16\pi/(1+q)^2$ , i.e. becomes smaller for more asymmetric systems.

FIG. 8. The area of the various horizons in BL data with different mass ratios as a function of the separation.

is a measure of excess radiative energy present between the horizon and spatial infinity. As we make  $d$  smaller and eventually set it to zero, we have just a single black hole and we recover a slice of the Schwarzschild spacetime (in isotropic coordinates). For a Schwarzschild black hole, since it is globally static, there is clearly no radiation and the horizon mass must equal the ADM mass. The horizon area is then just  $16\pi M_{\text{irr}}^2 = 16\pi M_{\text{ADM}}^2$ . Since we set  $M_{\text{ADM}} = 1$ , we expect that as  $d \rightarrow 0$ ,  $\text{Area} \rightarrow 16\pi \approx 50.265$ , which is what is found in Fig. 8(a) for all the mass ratios.

For the inner and the larger individual MOTS shown in Figs. 8(b) and 8(c), the areas are seen to increase monotonically as  $d$  is reduced. Clearly, just when the common horizon is formed, the inner MOTS and the AH coincide and their areas must necessarily agree. The inner MOTS area increases more rapidly and eventually has a larger area than the apparent horizon. The smaller horizon initially has a much smaller area than any of the other marginal surfaces. For  $d \rightarrow \infty$ , its irreducible mass must agree with the bare mass  $m_1$ . Thus, for a mass ratio  $q = m_2/m_1$ , we must have  $M_{\text{irr}} \approx 1/(1+q)$ , which implies that its area is approximately  $16\pi/(1+q)^2$ . Thus, the area is smaller for the more asymmetric system. For the larger MOTS, the same argument shows that the area must be  $16\pi q^2/(1+q)^2$  for large  $d$ . This is larger for more asymmetric systems.

For very small  $d$ , the area of the smaller MOTS increases very rapidly and the “small” black hole ends up having the largest area. This can be understood by recalling that the punctures are asymptotically flat regions by themselves. As the individual horizon nears the puncture, it is moving towards asymptotic infinity at the other end of the Einstein-Rosen bridge. It is thus not surprising that its area increases rapidly for very small  $d$ .

The next set of plots shows the maximum value of the intrinsic Ricci scalar on the horizons. As before, the apparent horizon is easy to understand. For a “round” sphere of radius  $R$  in Euclidean space, the scalar curvature is  $\mathcal{R} = 2/R^2$ . Following the same argument as above for the area we get  $\mathcal{R} = 8\pi/\text{Area} = 8\pi/(16\pi M_{\text{irr}}^2) \rightarrow 0.5$  as  $d \rightarrow 0$ . This is confirmed in Fig. 9(a). Similarly, the curvature of the smaller MOTS, which we have seen approaches asymptotic infinity and infinite radius, is  $\mathcal{R} = 2/R^2 \rightarrow 0$  as also seen in Fig. 9(d). For the inner MOTS, we have seen already in Fig. 6(b) that it is highly distorted and is almost pinching off at its neck. Thus, we expect increasingly large curvature at the neck, which is what is seen in Fig. 9(b). The behavior of the larger individual MOTS shown in Fig. 9(c) shows an interesting maximum for which we have no obvious explanation.

We can now postulate a scenario for the final fate of the remaining MOTS corresponding to the smaller black hole as  $d \rightarrow 0$ . For the exterior spacetime, in the “close-limit” approximation [70], for small  $d$  we should be able to express the exterior spacetime as a perturbation of the Schwarzschild solution. Thus we expect that the interior

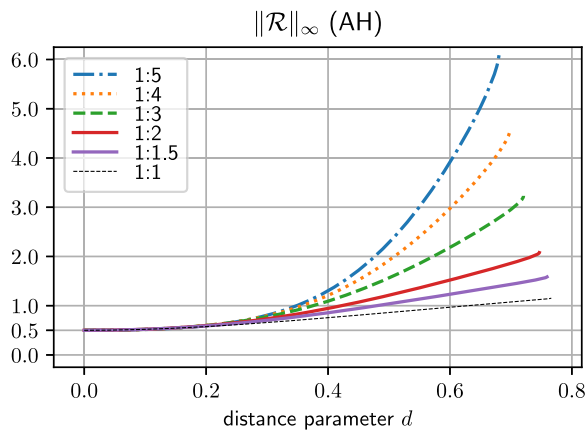
spacetime should also approach a slice of Schwarzschild in this limit. Since the coordinate radius of the MOTS vanishes asymptotically, it is plausible that the MOTS vanishes “into” the puncture, after which the puncture itself ceases to exist. Then we are just left with the other puncture so that asymptotically we have just a slice of Schwarzschild spacetime. This scenario could go wrong if the coordinate radius  $r$  of the MOTS (defined as the distance from the puncture to the location of the MOTS on the  $z$  axis towards the other puncture) does not decrease sufficiently rapidly with  $d$ , and the MOTS intersects the other puncture. Note that the proper distance will not be useful here since the proper distance from the puncture is always infinite. The question therefore is what happens to the ratio  $r/d$  as  $d \rightarrow 0$ . This is shown in Fig. 10. We see that  $r/d$  asymptotes to a constant value less than unity which supports the scenario outlined above. For the equal mass case,  $r/d \rightarrow 0$  as  $d \rightarrow 0$ , again showing that the equal mass case is qualitatively different.

## V. STABILITY AND EXISTENCE

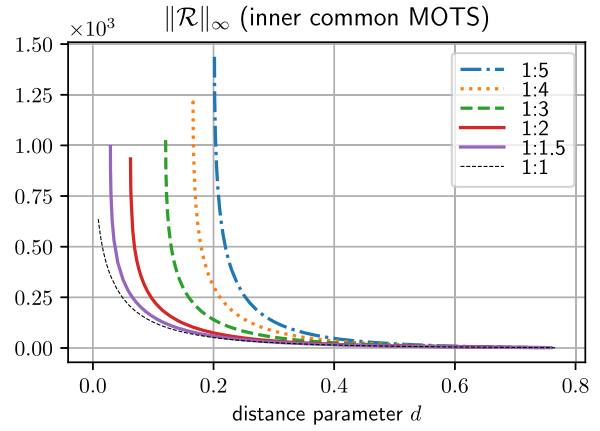
The previous section has illustrated some general properties of the different marginal surfaces for various values of the mass ratio. We have seen cases when the inner and larger marginal surfaces are not found or are highly distorted. The fundamental question of their existence and stability has been posed but we do not yet know why they cease to exist in certain cases. Are marginal surfaces inherently ill behaved or can these properties be understood in terms of predictable and regular quantities? In this section we answer these questions and show that there is a deep link between existence and stability. We shall start by trying to find the various MOTSs numerically as exhaustively as possible. Later we shall turn to the stability parameter to explain the failure to find some of these marginal surfaces.

We have already demonstrated the stability of the apparent horizon and the instability of the inner common MOTS in Fig. 7. We saw that the inner common MOTS  $\mathcal{S}_{\text{in}}$  is not a barrier between trapped and untrapped surfaces, and there exist constant expansion surfaces which lie on both sides of  $\mathcal{S}_{\text{in}}$ . Apart from this visual illustration, stability can be quantified by a real parameter. Recall that the stability of a MOTS is governed by the spectrum of the stability operator defined in Eq. (6). In particular, positivity of the principal eigenvalue guarantees smooth time evolution. The stability parameter is defined to be the principal eigenvalue which shall be discussed shortly.

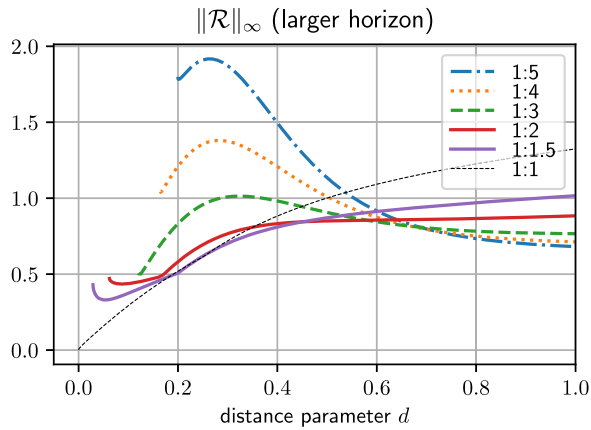
Since stability is connected with existence, we begin by investigating the critical values of  $d$  below which the inner and larger MOTSs,  $\mathcal{S}_{\text{in}}$  and  $\mathcal{S}_{\text{large}}$ , respectively, cease to exist. Since the apparent horizon and smaller individual MOTS exist for all  $d$  as we have seen, the question of existence is more relevant for the inner and larger MOTS. Figure 11 shows the critical values of  $d$ , denoted  $d_{\text{vanish}}$  for



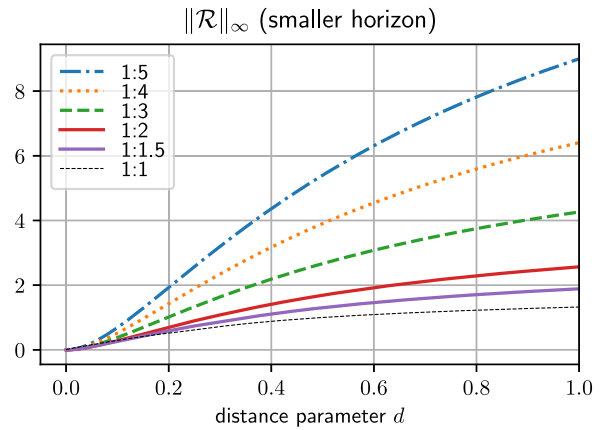
(a) The maximum of the Ricci scalar on the AH. For  $d \rightarrow 0$  this approaches 0.5, as expected for a “round” sphere.



(b) The inner common horizon becomes extremely distorted as  $d \rightarrow 0$ . This shows up as the sharp increase in the Ricci scalar right up to the point where the MOTS disappears.



(c) The Ricci scalar of the larger horizon. The discontinuous behavior of the slope of some of the curves is because there are multiple peaks, and it is possible for the maximum to go from one peak to the other.



(d) For  $d \rightarrow 0$  the smaller MOTS moves towards asymptotic infinity which is why its Ricci scalar vanishes asymptotically. The equal mass line is of course the same as the equal mass line in the previous panel Fig. 9c.

FIG. 9. The maximum value of the Ricci scalar on the various MOTSs in BL data with different mass ratios as a function of the separation. The purpose this plot is to give a rough quantitative idea about the distortions of the various marginal surfaces.

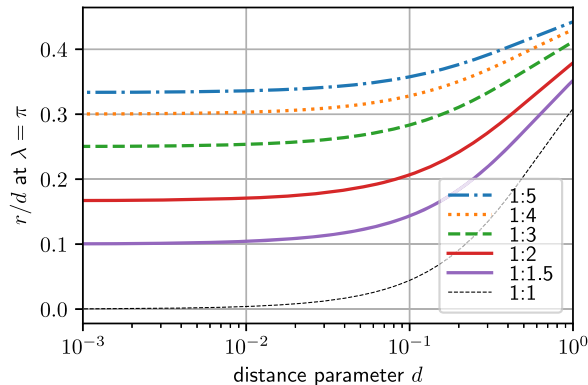


FIG. 10. The ratio of the coordinate radius of the smaller MOTS and the puncture separation  $d$ , as  $d$  approaches 0.

different mass ratios. The inner MOTS is seen to vanish just a little bit before the larger individual MOTS; i.e., the individual MOTS persists for slightly smaller values of  $d$ , and this is not a numerical artifact. It is not the case that these two surfaces touch each other just before vanishing. Referring again to the properties of minimal surfaces, if they did touch and their tangent vectors were aligned, then they would have had to coincide. In this case, the smaller MOTS acts as a barrier which prevents the  $\mathcal{S}_{in}$  and  $\mathcal{S}_{large}$  from touching.

To show this conclusively, we can compute the proper distance between  $\mathcal{S}_{in}$  and  $\mathcal{S}_{large}$  at their closest points of approach, namely along the negative  $z$  axis; see Fig. 12. This shows that the two surfaces never touch and are well separated just before they disappear compared to our numerical resolution.

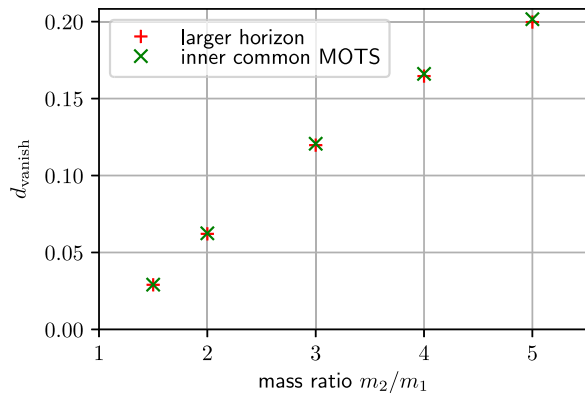


FIG. 11. The values of  $d$  for which the inner and larger MOTSs vanish for different mass ratios. The difference between the values for each mass ratio are small (but still much larger than numerical error). This is discussed in more detail in the next section (see Fig. 17 below). The equal mass case is qualitatively different and is not shown in this plot.

A search for constant expansion surfaces in the relevant region reveals an upper limit on the value of the expansion. As mentioned earlier in Sec. IV B 1, we find that we do not have any surfaces with  $\Theta_{(\ell)} > c$  for some negative constant  $c$ . To show this, we start with the AH which has of course zero expansion. Then we proceed in the inward direction finding surfaces with increasingly negative expansions. We can parameterize these surfaces also using their areas and we can plot the expansion as a function of the area. We expect that as we go inwards, we should initially have the expansion decreasing and becoming more negative. If the inner common MOTS exists, then this expansion must eventually start to increase. If it increases to zero, then we have found the inner common MOTS and we

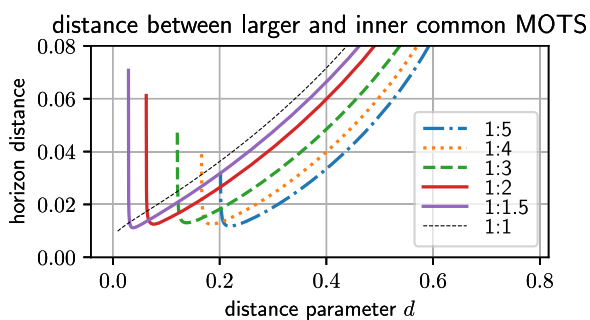


FIG. 12. The proper distance between  $\mathcal{S}_{\text{inner}}$  and  $\mathcal{S}_{\text{large}}$  as a function of  $d$ . As  $d$  is decreased, the proper distance decreases initially as one might expect. Surprisingly, this does not continue and the curve turns over, and the proper distance is increasing just before  $\mathcal{S}_{\text{inner}}$  vanishes. This shows that  $\mathcal{S}_{\text{inner}}$  and  $\mathcal{S}_{\text{large}}$  remain well separated from each other. The equal mass case is qualitatively different and in the limit of equal masses we must asymptotically get the purple curve. The calculations become more expensive as  $q \rightarrow 1$  and it is not entirely straightforward to understand this limit numerically.

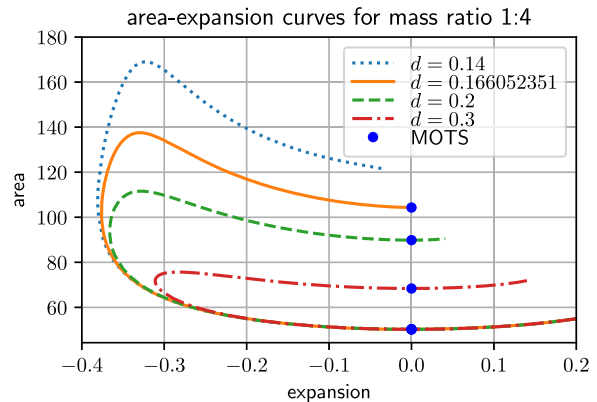


FIG. 13. Constant expansion surfaces parameterized by the value of the expansion and the area for mass ratio 1:4, for different values of  $d$ . See text for explanation.

should generally be able to extend the expansion to positive values. Taking the area as a function of the expansion, we should expect to find the MOTSs appear as local minima. As in Fig. 7, the constant expansion surfaces do not form a regular foliation and can intersect each other.

The results of this search for constant expansion surfaces are shown in Fig. 13. In this figure, the blue dots represent the MOTSs. The lowest blue dot is the AH. The curves with the different distance parameters do not actually coincide at that point, but, for the values of  $d$  that we have chosen, the areas are very close to each other and cannot be distinguished by eye on the plot [see also the curve for mass ratio 1:4 in Fig. 8(a)]. Going inwards from the AH corresponds to moving leftwards from the AH and the curves for different  $d$  can soon be differentiated. All the curves eventually turn over and the expansion starts to increase towards 0. However, not all the curves actually reach 0; e.g., for  $d = 0.14$  the curve stops well before that. Thus, for  $d = 0.14$ , not only are we unable to find surfaces of zero expansion, we also cannot find any surfaces with  $\Theta_{(\ell)} > c$  for some *negative* number  $c$ . At the critical value, the curve stops precisely at 0 and for larger  $d$  the curves extend to positive expansions. In each case, the MOTSs all occur at local minima of the area.

Based on this detailed numerical study, we are led to suspect that the inner and larger MOTS simply cease to exist below critical values of  $d$ . Since it is inherently difficult to show that something does not exist, is this a limitation of our numerical method? Would we continue to find these marginal surfaces if only we looked even more carefully?

### A. The stability parameter

To answer this question, we turn now to the stability operator defined in Sec. II A. As mentioned there, the sign of the principal eigenvalue is important. The positivity of this principal eigenvalue implies stable time evolution and

should thus also be relevant to the question of whether the surfaces can be found in Cauchy data. We denote the principal eigenvalue as the *stability parameter*. Before presenting numerical results, it is useful to briefly describe what we might expect theoretically, and in particular what kind of MOTSs are expected to have negative stability parameter. It can be shown that, for vacuum time-symmetric data, the stability operator of Eqs. (6) and (7) can be written as

$$Lf = -\Delta f + \frac{\mathcal{R}}{2}f. \quad (32)$$

As before,  $\mathcal{R}$  is the intrinsic Ricci scalar on  $\mathcal{S}$ . The spectrum of the Laplacian on a general distorted sphere can be very complicated and from a full knowledge of the spectrum we can infer some geometrical properties of  $\mathcal{S}$  such as its area and its genus (see e.g., [71,72]). Asymptotic properties of the spectrum are also known but here we shall need the lower eigenvalues. Regarding the MOTS stability operator itself, Jaramillo [73–75] has pointed out the relevance of studying its full spectrum in the context of generic MOTS dynamics. An interesting physical interpretation of the stability operator as a “pressure operator” is presented in [73], and [74] connects it with the problem of a quantum charged particle. The stability operator is also related to extremality [75,76]. Numerical studies should be able to extend these results and lead to a better understanding of the stability operator in generic situations.

Some obvious simplifications are possible in special cases. For a “round” 2-sphere, with  $\mathcal{R} = 2/R^2$ , the principal eigenvalue is simply

$$\Lambda_0 = \frac{1}{R^2} = \frac{1}{4M_{\text{irr}}^2}. \quad (33)$$

This will be relevant for the AH as  $d \rightarrow 0$ , and for the individual horizons as  $d \rightarrow \infty$ . Thus, round spheres are always stable and it follows then that the inner MOTS cannot be spherically symmetric. The higher eigenvalues are easily obtained from the spectrum of the Laplacian on a sphere of radius  $R$ , i.e.,  $\Lambda_n = [1 + n(n+1)]/R^2$ ,  $n = 0, 1, 2, 3, \dots$ , with multiplicity  $2n+1$ .

More generally in the absence of any symmetries, from the Rayleigh-Ritz formula, if  $\psi$  is a square integrable function (with unit norm) on  $\mathcal{S}$ ,

$$\Lambda_0 = \inf_{\psi} \int_{\mathcal{S}} \left( \|\partial\psi\|^2 + \frac{1}{2}\mathcal{R}\psi^2 \right) d^2V. \quad (34)$$

Thus, we are more likely to get instabilities when there are significant regions of negative curvature on  $\mathcal{S}$ ; in fact, there *must* be regions of negative curvature for unstable marginal surfaces. The work of [46–48] also uses the Rayleigh-Ritz formula, albeit a generalized version valid for the non-self-adjoint case.

We now present our numerical results for the stability parameter. Plots of the stability parameter are shown in Fig. 14 for all four kinds of marginal surfaces as a function of  $d$ . These plots have several very interesting features which we now discuss.

First, the apparent horizon is always seen to be stable as expected in Fig. 14(a). When it is first formed, its stability parameter is zero but it rapidly increases before leveling off. Its asymptotic value is 0.25, consistent with the above argument for  $\Lambda_0$  since its irreducible mass approaches unity. Similarly, in Fig. 14(d) the smaller MOTS remains stable as it grows, and its stability parameter vanishes asymptotically (consistent again with it vanishing in the limit  $d \rightarrow 0$ ).

The other two horizons are particularly interesting. The stability parameter for the larger individual MOTS is positive [Fig. 14(c)]. Remarkably, it ceases to exist exactly when the stability parameter vanishes. This shows that the absence of this MOTS below a critical value of  $d$  is not an accident and is not a limitation of our numerical method. This confirms the link between stability and existence for this MOTS.

Now we turn to the inner common MOTS. It is born with zero stability parameter and, of course, it coincides with the apparent horizon at birth. The stability parameter is strictly negative for smaller values of  $d$ , and it decreases monotonically as  $d$  is decreased; see Fig. 14(b). A close-up of the regime when the common MOTSs are just formed is shown in Fig. 15, demonstrating the bifurcation of the common MOTS into two branches.

Does the existence of this MOTS, for which the stability parameter is always negative and decreasing, cast doubt on the relevance of the stability operator? To investigate this, we go back to the work of Andersson *et al.* [46–48]. The important issue is whether the stability operator is invertible; i.e., we need to ensure that zero eigenvalue states are not allowed. This is guaranteed automatically when the principal eigenvalue is positive. In the case when the principal eigenvalue is negative, we must require that none of the higher eigenvalues vanish. More specifically, since the principle eigenvalue is initially zero and decreases monotonically, we need only investigate the second eigenvalue. When the MOTS is formed, it must be positive. The question then is: does it decrease and does it ever vanish and then become negative? Figure 16 shows the second eigenvalue as a function of  $d$  for the different mass ratios. Even more remarkably, we see that this eigenvalue vanishes *exactly* at the point when the inner common MOTS vanishes. Again, this supports our claim that the MOTS does not exist for small  $d$  and that its disappearance is not merely a limitation of our numerical method. More importantly, we see again the importance of the stability operator to the question of the existence of marginal surfaces.

Finally, going back to the question of whether the inner and larger MOTS vanish at different times (Fig. 11), we can

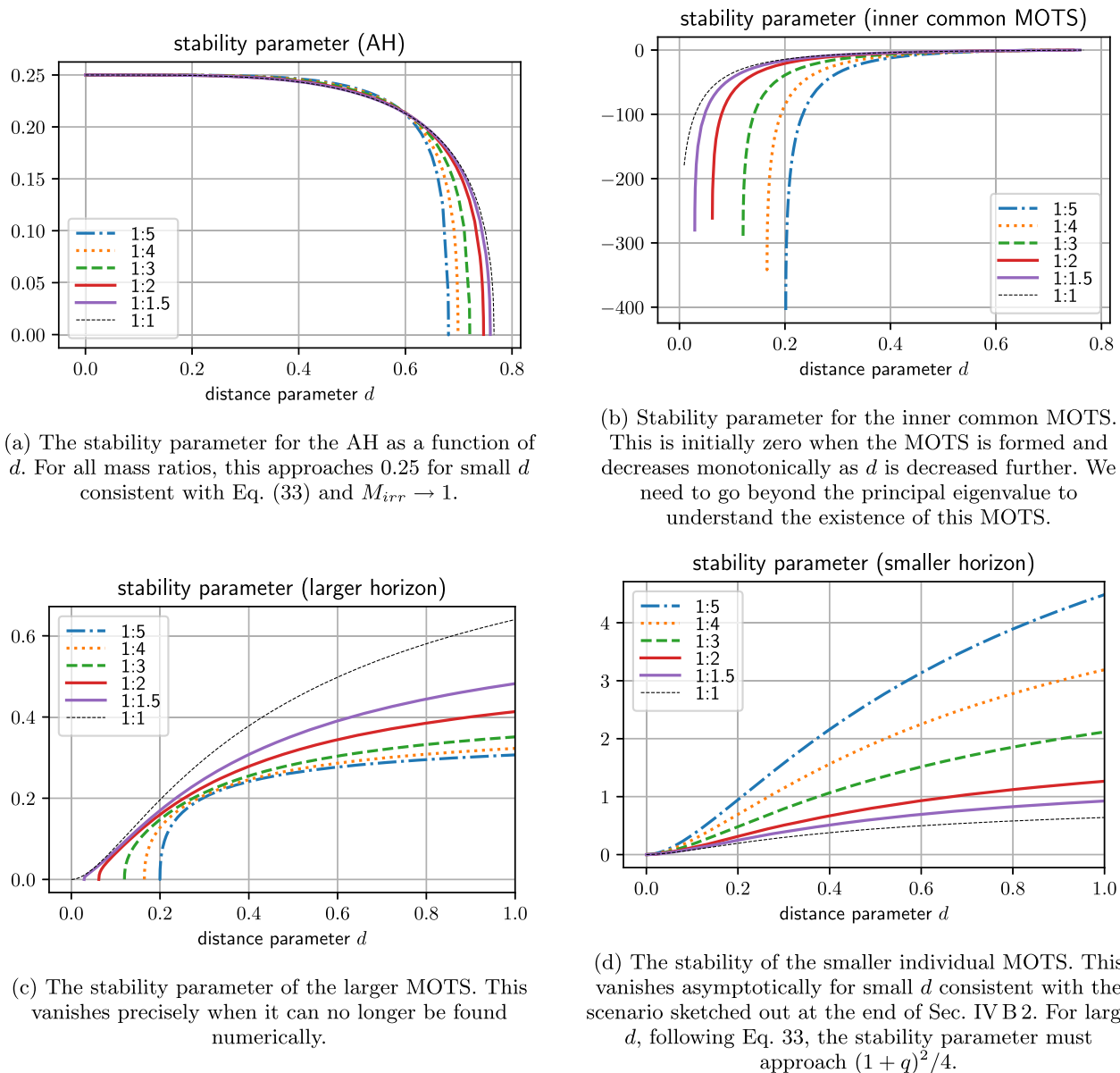


FIG. 14. The stability parameter for MOTSs in BL data with different mass ratios as a function of the separation.

look at when the stability parameter for the larger MOTS and the second eigenvalue for the inner common MOTS vanish. Figure 17 shows the principal eigenvalue for the larger MOTS and the second eigenvalue for the inner common MOTS. Both of these eigenvalues vanish but at different values of  $d$ . This confirms again that the inner common MOTS vanishes before the larger individual MOTS.

## VI. THE MASS MULTIPOLES

The geometric mass multipole moments  $I_n$  have been defined previously in Eq. (8). We can apply this to any of the MOTSs that we have found, but it is the most interesting to calculate them for the apparent horizon. As described

in [28], these moments approach their final stationary values (in general corresponding to a Kerr black hole), and it is of interest to calculate the rate at which they decay. In the present case, the “final” black hole is Schwarzschild and  $d$  is a proxy for time. Thus, except  $I_0$  (which is a geometric invariant), we expect all the  $I_n$  to vanish asymptotically as  $d \rightarrow 0$ .

Figure 18 shows the mass multipole moments for the 1:4 configuration as a function of  $d$ . The lowest moment  $I_0$  is a geometric invariant, the integral of the Ricci scalar over  $\mathcal{S}$ . The Gauss-Bonnet theorem shows that  $I_0 = \sqrt{\pi}$  for a sphere. We see next that the mass dipole  $I_1$  vanishes. This is true generally as shown in [61], with the physical interpretation being that the invariant coordinates automatically place us in the center-of-mass frame of the

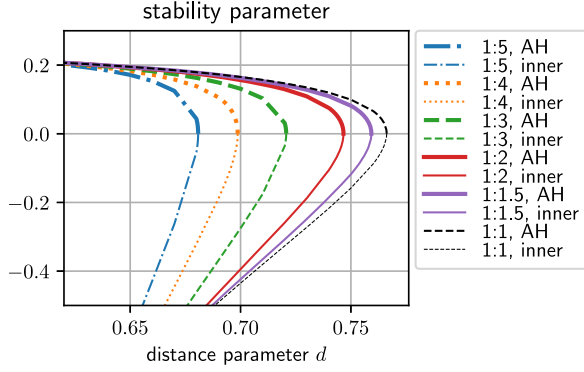


FIG. 15. The stability parameters of the apparent horizon and the inner common MOTS near the point of formation for different mass ratios. We see clearly the formation and bifurcation of the marginal surfaces into a stable and unstable branch.

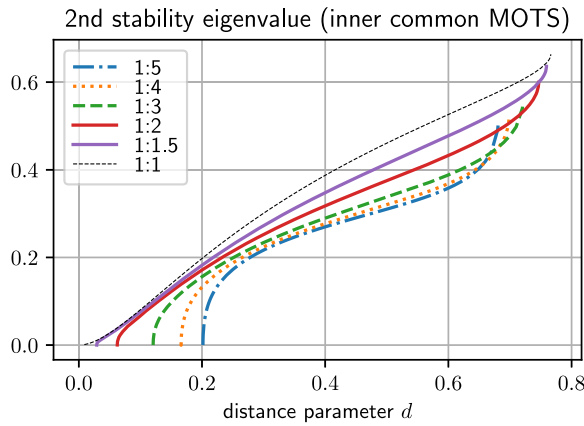


FIG. 16. The second eigenvalue of the stability operator for the inner horizon for different mass ratios. This MOTS ceases to exist precisely when the second eigenvalue vanishes. As in many of the other plots, the equal mass ratio case is qualitatively different in that the individual MOTSs continue to exist and become unstable only asymptotically as  $d \rightarrow 0$ . This limit is however not easy to explore numerically.

horizon. For all  $n \geq 2$ , Fig. 18 shows that the  $I_n$  fall off as power laws as  $d \rightarrow 0$  and it turns out that this falloff rate is *independent* of the mass ratio. This is similar to what one expects in a time evolution. When a distorted horizon is initially formed, its initial configuration and which moments are excited depends on the data which produced the horizon. Thus, in a binary black-hole system, this would depend on the mass ratio, spin configurations, etc. However, the approach to equilibrium has universal properties and this is reflected in the falloff of the  $I_n$ . A simple numerical fit of the numerical data for mass ratio 1:4 and other mass ratios gives

$$I_n \propto d^n, \quad n \geq 2. \quad (35)$$

We have verified this for  $n \leq 7$ . Whether this behavior carries over to time evolutions remains to be seen.

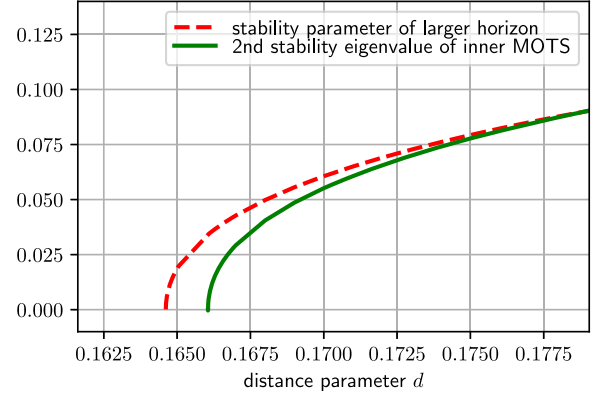


FIG. 17. The second eigenvalue of the stability operator for the inner common MOTS and the principal eigenvalue for the larger individual horizon for mass ratio 1:4. Both these curves have appeared in earlier plots, but here we show them close to where the surfaces cease to exist. We see that the eigenvalues both vanish and do so at different values of  $d$ . The large MOTS persists somewhat longer than the inner common one. Similar results hold for the other mass ratios.

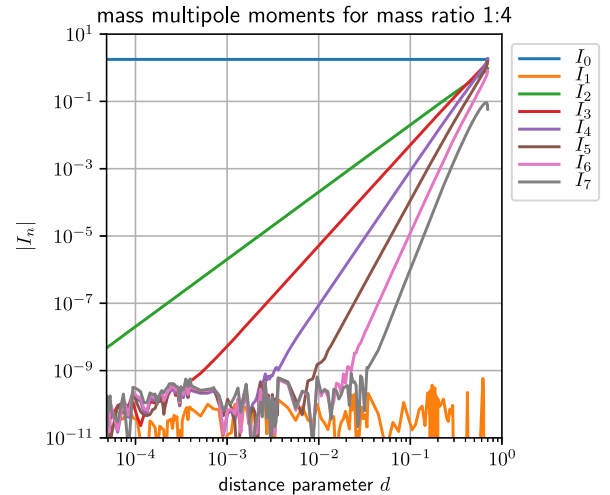


FIG. 18. Mass multipoles  $|I_n|$  of the apparent horizon as a function of the distance. Values below  $10^{-9}$  are in the numerical noise. This plot is for the 1:4 mass ratio configuration; however, the falloff rates with  $d$  do not depend on the mass ratio. The first moment  $I_0 = \sqrt{\pi}$  is a geometric invariant, and the others fall off as  $I_n \sim d^n$ .

## VII. CONCLUSIONS

The stability operator is known to be very important in mathematical studies of marginally trapped surfaces. Among other results, it shows the link between stability and smoothness under time evolution. It also controls other properties of a MOTS in a given time slice, such as its behavior as a barrier for completely trapped and untrapped surfaces. In this paper we have shown the importance of the stability operator for understanding marginally trapped surfaces in numerical calculations. By monitoring the

lowest eigenvalues of the stability operator, we can effectively diagnose whether any problems might be expected in the horizon finder or in the time evolution. In the case when the principal eigenvalue is already negative, then the second eigenvalue must be considered. The horizon will cease to exist when this second eigenvalue vanishes.

In general, the stability operator is not self-adjoint. Thus, apart from the principal eigenvalue, higher eigenvalues can be complex. It is easier for them to avoid the origin even if their real parts vanish. For the inner horizon in generic cases when the principal eigenvalue is already negative, it is not clear if there is any reason for the eigenvalues to precisely vanish. It might also happen that instabilities can arise when the eigenvalues get sufficiently close to 0. Following up on the results presented here, these questions will be investigated in forthcoming work.

Another important part of this paper is a new numerical algorithm and its implementation for locating MOTSs capable of finding highly distorted surfaces with no additional computational cost. The method is a modification of the commonly used AHFinderDirect and is based on choosing a reference surface. We have implemented a pseudospectral scheme to represent the surface and we use a Newton-Kantorovich method for solving the resulting nonlinear PDE. This implementation is at present valid in axisymmetry, but no in-principle difficulty is foreseen for the full three-dimensional case. This will be incorporated into the Einstein Toolkit software and thus available generally for black-hole simulations.

We have applied this method to sequences of Brill-Lindquist data as the separation between the puncture is decreased and a rich structure of marginal surfaces is explored. The distance parameter  $d$  can be pushed to 0 and

some of the inner marginal surfaces become highly distorted. Our horizon finder is able to locate these with high accuracy. The stability parameter works as advertised: the larger individual horizon ceased to exist precisely when its stability parameter vanishes. The inner horizon is born with zero stability parameter and it decreases monotonically as  $d$  is decreased. The second eigenvalue thus becomes relevant and this MOTS disappears exactly when this second eigenvalue vanishes. Distorted as they are, the MOTSs are successfully tracked by our new numerical horizon finder all the way to their disappearance due to losing physical stability.

Finally, we have found universal behavior (i.e., independent of the mass ratio) of the mass multipole moments in the limit  $d \rightarrow 0$ . Forthcoming work will apply this horizon finder to time evolutions. One of the goals will be to find the fate of the inner horizons in binary black-hole spacetimes and to verify if this universality in the approach to the final state still holds.

## ACKNOWLEDGMENTS

We thank Bruce Allen, Abhay Ashtekar, Jose-Luis Jaramillo, Istvan Racz and Jeff Winicour for valuable discussions. We are especially grateful to Lars Andersson for pointing out the importance of the invertibility of the stability operator to us. O. B. acknowledges the National Science Foundation (NSF) for financial support from Grant No. PHY-1607520. The research was also supported by the Perimeter Institute for Theoretical Physics. Research at Perimeter Institute is supported by the Government of Canada through Industry Canada and by the Province of Ontario through the Ministry of Research and Innovation.

- 
- [1] T. Baumgarte and T. Shapiro, *Numerical Relativity: Solving Einstein's Equations on the Computer* (Cambridge University Press, Cambridge, England, 2010).
  - [2] M. Shibata, *Numerical Relativity (100 Years of Relativity)* (World Scientific, Singapore, 2016), Vol. 1.
  - [3] M. Alcubierre, *Introduction to 3+1 Numerical Relativity* (Oxford University Press, Oxford, 2008).
  - [4] B. P. Abbott *et al.* (Virgo and LIGO Scientific Collaborations), Directly comparing GW150914 with numerical solutions of Einsteins equations for binary black hole coalescence, *Phys. Rev. D* **94**, 064035 (2016).
  - [5] F. Pretorius, Evolution of Binary Black Hole Spacetimes, *Phys. Rev. Lett.* **95**, 121101 (2005).
  - [6] M. Campanelli, C. O. Lousto, P. Marronetti, and Y. Zlochower, Accurate Evolutions of Orbiting Black-Hole Binaries without Excision, *Phys. Rev. Lett.* **96**, 111101 (2006).
  - [7] J. G. Baker, J. Centrella, D.-I. Choi, M. Koppitz, and J. van Meter, Gravitational Wave Extraction from an Inspiral Configuration of Merging Black Holes, *Phys. Rev. Lett.* **96**, 111102 (2006).
  - [8] Y. Zlochower, J. G. Baker, M. Campanelli, and C. O. Lousto, Accurate black hole evolutions by fourth-order numerical relativity, *Phys. Rev. D* **72**, 024021 (2005).
  - [9] J. Healy, C. O. Lousto, and Y. Zlochower, Remnant mass, spin, and recoil from spin aligned black-hole binaries, *Phys. Rev. D* **90**, 104004 (2014).
  - [10] A. Čadež, Apparent horizons in the two-black-hole problem, *Ann. Phys. (N.Y.)* **83**, 449 (1974).
  - [11] P. Anninos, D. Bernstein, S. R. Brandt, D. Hobill, E. Seidel, and L. Smarr, Dynamics of black hole apparent horizons, *Phys. Rev. D* **50**, 3801 (1994).
  - [12] P. Anninos, K. Camarda, J. Libson, J. Massó, E. Seidel, and W.-M. Suen, Finding apparent horizons in dynamic

- 3D numerical spacetimes, *Phys. Rev. D* **58**, 024003 (1998).
- [13] D. M. Shoemaker, M. F. Huq, and R. A. Matzner, Generic tracking of multiple apparent horizons with level flow, *Phys. Rev. D* **62**, 124005 (2000).
- [14] M. F. Huq, M. W. Choptuik, and R. A. Matzner, Locating boosted Kerr and Schwarzschild apparent horizons, *Phys. Rev. D* **66**, 084024 (2002).
- [15] J. Thornburg, A fast apparent-horizon finder for 3-Dimensional Cartesian grids in numerical relativity, *Classical Quantum Gravity* **21**, 743 (2004).
- [16] E. Schnetter, F. Herrmann, and D. Pollney, Horizon Pre-tracking, *Phys. Rev. D* **71**, 044033 (2005).
- [17] R. Penrose, Gravitational Collapse and Space-Time Singularities, *Phys. Rev. Lett.* **14**, 57 (1965).
- [18] S. W. Hawking and R. Penrose, The Singularities of gravitational collapse and cosmology, *Proc. R. Soc. A* **314**, 529 (1970).
- [19] A. Ashtekar and B. Krishnan, Isolated and dynamical horizons and their applications, *Living Rev. Relativity* **7**, 10 (2004).
- [20] I. Booth, Black hole boundaries, *Can. J. Phys.* **83**, 1073 (2005).
- [21] E.ourgoulhon and J. L. Jaramillo, A 3 + 1 perspective on null hypersurfaces and isolated horizons, *Phys. Rep.* **423**, 159 (2006).
- [22] S. A. Hayward, Energy and entropy conservation for dynamical black holes, *Phys. Rev. D* **70**, 104027 (2004).
- [23] J. L. Jaramillo, An introduction to local black hole horizons in the 3 + 1 approach to general relativity, *Int. J. Mod. Phys. D* **20**, 2169 (2011).
- [24] B. Krishnan, Quasi-local black hole horizons, in *Springer Handbook of Spacetime*, edited by A. Ashtekar and V. Petkov (Springer-Verlag, Berlin, 2014), pp. 527–555.
- [25] B. Krishnan, Fundamental properties and applications of quasi-local black hole horizons, *Classical Quantum Gravity* **25**, 114005 (2008).
- [26] O. Dreyer, B. Krishnan, D. Shoemaker, and E. Schnetter, Introduction to isolated horizons in numerical relativity, *Phys. Rev. D* **67**, 024018 (2003).
- [27] E. Schnetter, B. Krishnan, and F. Beyer, Introduction to dynamical horizons in numerical relativity, *Phys. Rev. D* **74**, 024028 (2006).
- [28] A. Gupta, B. Krishnan, A. Nielsen, and E. Schnetter, Dynamics of marginally trapped surfaces in a binary black hole merger: Growth and approach to equilibrium, *Phys. Rev. D* **97**, 084028 (2018).
- [29] J. D. Bekenstein, Black holes and entropy, *Phys. Rev. D* **7**, 2333 (1973).
- [30] J. D. Bekenstein, Generalized second law of thermodynamics in black hole physics, *Phys. Rev. D* **9**, 3292 (1974).
- [31] J. D. Bekenstein and A. Meisels, Einstein *A* and *B* coefficients for a black hole, *Phys. Rev. D* **15**, 2775 (1977).
- [32] J. M. Bardeen, B. Carter, and S. W. Hawking, The Four laws of black hole mechanics, *Commun. Math. Phys.* **31**, 161 (1973).
- [33] S. W. Hawking, Gravitational Radiation from Colliding Black Holes, *Phys. Rev. Lett.* **26**, 1344 (1971).
- [34] V. Faraoni and A. Prain, Cosmological and black hole apparent horizons, *Lect. Notes Phys.* **907**, 1 (2015).
- [35] M. Visser, Physical observability of horizons, *Phys. Rev. D* **90**, 127502 (2014).
- [36] S. A. Hayward, Black holes: New horizons, [arXiv:gr-qc/0008071](https://arxiv.org/abs/gr-qc/0008071).
- [37] M. Cabero, C. D. Capano, O. Fischer-Birnholtz, B. Krishnan, A. B. Nielsen, A. H. Nitz, and C. M. Biwer, Observational tests of the black hole area increase law, *Phys. Rev. D* **97**, 124069 (2018).
- [38] I. Booth, L. Brits, J. A. Gonzalez, and C. Van Den Broeck, Marginally trapped tubes and dynamical horizons, *Classical Quantum Gravity* **23**, 413 (2006).
- [39] J. L. Jaramillo, M. Ansorg, and N. Vasset, Application of initial data sequences to the study of black hole dynamical trapping horizons, *AIP Conf. Proc.* **1122**, 308 (2009).
- [40] C. Williams, Asymptotic behavior of spherically symmetric marginally trapped tubes, *Ann. Henri Poincaré* **9**, 1029 (2008).
- [41] C. Williams, A black hole with no marginally trapped tube asymptotic to its event horizon, [arXiv:1005.5401](https://arxiv.org/abs/1005.5401).
- [42] J. L. Jaramillo, R. P. Macedo, P. Mösta, and L. Rezzolla, Black-hole horizons as probes of black-hole dynamics I: Post-merger recoil in head-on collisions, *Phys. Rev. D* **85**, 084030 (2012).
- [43] J. L. Jaramillo, R. P. Macedo, P. Mösta, and L. Rezzolla, Black-hole horizons as probes of black-hole dynamics II: Geometrical insights, *Phys. Rev. D* **85**, 084031 (2012).
- [44] J. L. Jaramillo, R. P. Macedo, P. Mösta, and L. Rezzolla, Towards a cross-correlation approach to strong-field dynamics in black hole spacetimes, *AIP Conf. Proc.* **1458**, 158 (2012).
- [45] L. Rezzolla, R. P. Macedo, and J. L. Jaramillo, Understanding the ‘Anti-Kick’ in the Merger of Binary Black Holes, *Phys. Rev. Lett.* **104**, 221101 (2010).
- [46] L. Andersson, M. Mars, and W. Simon, Local Existence of Dynamical and Trapping Horizons, *Phys. Rev. Lett.* **95**, 111102 (2005).
- [47] L. Andersson, M. Mars, and W. Simon, Stability of marginally outer trapped surfaces and existence of marginally outer trapped tubes, *Adv. Theor. Math. Phys.* **12**, 853 (2008).
- [48] L. Andersson, M. Mars, J. Metzger, and W. Simon, The time evolution of marginally trapped surfaces, *Classical Quantum Gravity* **26**, 085018 (2009).
- [49] I. Booth and S. Fairhurst, Isolated, slowly evolving, and dynamical trapping horizons: geometry and mechanics from surface deformations, *Phys. Rev. D* **75**, 084019 (2007).
- [50] R. Bousso and N. Engelhardt, Proof of a new area law in general relativity, *Phys. Rev. D* **92**, 044031 (2015).
- [51] R. Bousso and N. Engelhardt, New Area Law in General Relativity, *Phys. Rev. Lett.* **115**, 081301 (2015).
- [52] J. Thornburg, Event and apparent horizon finders for 3 + 1 numerical relativity, *Living Rev. Relativity* **10**, 3 (2007).
- [53] F. Löffler, J. Faber, E. Bentivegna, T. Bode, P. Diener, R. Haas, I. Hinder, B. C. Mundim, C. D. Ott, E. Schnetter, G. Allen, M. Campanelli, and P. Laguna, The Einstein toolkit: A community computational infrastructure for relativistic astrophysics, *Classical Quantum Gravity* **29**, 115001 (2012).

- [54] EinsteinToolkit, Einstein toolkit: Open software for relativistic astrophysics, <http://einsteintoolkit.org/>.
- [55] U. Hussain and I. Booth, Deformation of horizons during a merger, *Classical Quantum Gravity* **35**, 015013 (2018).
- [56] P. Figueras, M. Kunesch, L. Lehner, and S. Tunyasuvunakool, End Point of the Ultraspinning Instability and Violation of Cosmic Censorship, *Phys. Rev. Lett.* **118**, 151103 (2017).
- [57] R. M. Wald and V. Iyer, Trapped surfaces in the Schwarzschild geometry and cosmic censorship, *Phys. Rev. D* **44**, R3719 (1991).
- [58] E. Schnetter and B. Krishnan, Non-symmetric trapped surfaces in the Schwarzschild and Vaidya spacetimes, *Phys. Rev. D* **73**, 021502 (2006).
- [59] I. Booth, H. K. Kunduri, and A. O'Grady, Unstable marginally outer trapped surfaces in static spherically symmetric spacetimes, *Phys. Rev. D* **96**, 024059 (2017).
- [60] R. P. A. C. Newman, Topology and stability of marginal 2-surfaces, *Classical Quantum Gravity* **4**, 277 (1987).
- [61] A. Ashtekar, J. Engle, T. Pawłowski, and C. Van Den Broeck, Multipole moments of isolated horizons, *Classical Quantum Gravity* **21**, 2549 (2004).
- [62] A. Ashtekar and B. Krishnan, Dynamical horizons and their properties, *Phys. Rev. D* **68**, 104030 (2003).
- [63] J. Boyd, *Chebyshev and Fourier Spectral Methods* (Dover Publications, New York, 2001).
- [64] C. Canuto, M. Yousuff Hussaini, A. Quarteroni, and T. A. Zang, *Spectral Methods: Fundamentals in Single Domains* (Springer-Verlag, Berlin, 2006).
- [65] D. R. Brill and R. W. Lindquist, Interaction energy in geometrostatics, *Phys. Rev.* **131**, 471 (1963).
- [66] P. Mösta, L. Andersson, J. Metzger, B. Szilágyi, and J. Winicour, The merger of small and large black holes, *Classical Quantum Gravity* **32**, 235003 (2015).
- [67] B. Krishnan, Isolated horizons in numerical relativity, Ph.D. thesis, Pennsylvania State University, 2002.
- [68] N. Lages, Apparent horizons and marginally trapped surfaces in numerical general relativity, Ph.D. thesis, Friedrich-Schiller-Universität Jena, 2010.
- [69] E. Schnetter, Finding apparent horizons and other two surfaces of constant expansion, *Classical Quantum Gravity* **20**, 4719 (2003).
- [70] R. H. Price and J. Pullin, Colliding Black Holes: The Close Limit, *Phys. Rev. Lett.* **72**, 3297 (1994).
- [71] S. Minakshisundaram and A. Pleijel, Some properties of the eigenfunctions of the Laplace operator on Riemannian manifolds, *Can. J. Math.* **1**, 242 (1949).
- [72] M. Kac, Can one hear the shape of a drum?, *Am. Math. Mon.* **73**, 1 (1966).
- [73] J. L. Jaramillo, A Young-Laplace law for black hole horizons, *Phys. Rev. D* **89**, 021502 (2014).
- [74] J. L. Jaramillo, Black hole horizons and quantum charged particles, *Classical Quantum Gravity* **32**, 132001 (2015).
- [75] J. L. Jaramillo, A note on degeneracy, marginal stability and extremality of black hole horizons, *Classical Quantum Gravity* **29**, 177001 (2012).
- [76] M. Mars, Stability of MOTS in totally geodesic null horizons, *Classical Quantum Gravity* **29**, 145019 (2012).